

Formic Acid Dehydration Rates and Elementary Steps on Lewis Acid–Base Site Pairs at Anatase and Rutile TiO₂ Surfaces

Stephanie Kwon, Ting Chun Lin, and Enrique Iglesia*

Cite This: *J. Phys. Chem. C* 2020, 124, 20161–20174

Read Online

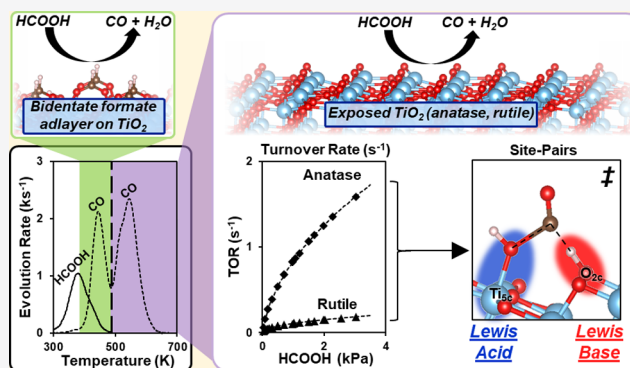
ACCESS |

Metrics & More

Article Recommendations

Supporting Information

ABSTRACT: Formic acid (HCOOH) decomposition is often used to assess the acid–base properties of oxide surfaces. Its reverse reaction forms HCOOH and formate species that can act as intermediates in CO₂/CO/H₂/H₂O reactions that are important in C₁ conversions. This study describes the mechanism of HCOOH dehydration on acid–base pairs at anatase and rutile TiO₂ surfaces through spectroscopic, desorption–reaction, kinetic, isotopic, and theoretical methods. HCOOH dehydration turnover rates are measured at coverages that allow bound intermediates to interact directly with Ti_{5c}–O_{2c} pairs. Such rates then reflect their acid–base properties without interference from a refractory bidentate formate adlayer that acts as the catalytic surface at lower temperatures, as evident from infrared and desorption reaction data. HCOOH dehydration elementary steps involve the concurrent activation of C–O and C–H bonds in a molecularly bound HCOOH (HCOOH*) by a Ti_{5c}–O_{2c} pair at the kinetically relevant step. The transition state mediating this step involves the OH group and the H-atom of the C–H group in HCOOH* that are almost fully transferred to the Ti_{5c} and the vicinal O_{2c} center, respectively. Such concerted interactions with the acid and base centers and the late character of the transition state render the H₂O dissociation energy at Ti_{5c}–O_{2c} pairs a more suitable descriptor of HCOOH reactivity than the respective strengths of each Lewis center. These mechanistic conclusions allow quantitative inferences of the rate and kinetic parameters for HCOOH synthesis from CO–H₂O reactants on TiO₂ surfaces through the tenets of microscopic reversibility extended to the sequence of elementary steps. The results also illustrate how acid–base pairs act in concert to stabilize the relevant transition states, thus making the balance between acid and base strengths, instead of their independent properties, the rigorous arbiters of reactivity, as shown by the similar reactivities and H₂O dissociation energies on Ti_{5c}–O_{2c} pairs at anatase and rutile surfaces in spite of their very different acid and base strengths.



1. INTRODUCTION

Formic acid (HCOOH) decomposes on metals and oxides via dehydrogenation (to CO₂ and H₂) and dehydration (to CO and H₂O). These routes and their reverse pathways, which form HCOOH and formate-type intermediates from CO, CO₂, H₂, and H₂O mixtures, may play a role in mediating catalytic C₁ chemistries involved in CO₂ reduction,¹ water–gas shift (WGS),² and methanol synthesis.^{3,4} HCOOH decomposition routes on metals (e.g., Cu,⁵ Ni,⁶ Au,⁷ Pd,⁸ and Pt⁹) that predominantly form CO₂ and H₂ via bound bidentate formates (*HCOO*) have been previously examined using experimental and theoretical methods. In contrast, mechanistic proposals for metal oxides are much more diverse and complex. Basic oxides, such as MgO,¹⁰ form CO₂ and H₂, while Al₂O₃¹¹ and TiO₂^{12,13} predominantly form CO and H₂O. The effects of acid–base oxide properties on HCOOH decomposition reactivity and selectivity remain controversial, even though such properties are often used as phenomenological descriptors of these properties¹⁴ and the relevant oxides are frequently used as promoters for many C₁ reactions.

Oxides with high HCOOH dehydration reactivity (e.g., CeO₂¹⁵ and TiO₂^{13,16}), and by reversibility inferences also high rates for CO–H₂O reactions that form HCOOH, promote WGS^{17,18} reactions when combined with metal functions (e.g., Pt⁹ and Au⁷) that favor HCOOH dehydrogenation (and by inference CO₂–H₂ reactions that form HCOOH). Such metal–oxide pairings may reflect CO–H₂O paths that form HCOOH on oxide promoters and HCOOH dehydrogenation (to CO₂ and H₂) on the metal function, thus completing WGS turnovers in tandem reactions using HCOOH as a gaseous molecular shuttle. Similarly, the combination of CO₂–H₂ reactions that form HCOOH and a HCOOH hydrolysis

Received: June 23, 2020

Revised: July 31, 2020

Published: September 1, 2020



function that forms CH_3OH provides facile low-temperature methanol synthesis routes on organometallic complexes, albeit at very high CO_2 and H_2 pressures, to allow practical equilibrium concentrations of HCOOH molecular shuttles.^{19,20}

The assessment of the strength of acid–base centers and their role in HCOOH dehydration requires unequivocal mechanistic understanding of the identity and kinetic relevance of elementary steps and bound species. Such assessments are often hindered by the ubiquitous presence of a refractory template of the bound $^*\text{HCOO}^*$ species that act as the “active surface” during catalytic turnovers, thus obscuring how the inherent properties of acid–base pairs influence HCOOH decomposition. At relatively low temperatures (423–463 K), HCOOH dehydration turnovers do occur but on $^*\text{HCOO}^*$ -saturated TiO_2 surfaces. As a result, their rates reflect indirectly, at best, the binding properties of acid–base site pairs that act as the substrate for the refractory $^*\text{HCOO}^*$ template upon which turnovers occur, as shown in a previous study.¹³

At higher temperatures, HCOOH dehydration turnovers occur directly on acid–base site pairs at TiO_2 surfaces, leading to detectable inferences about the relations between their binding properties and reactivity. Anatase [$\text{TiO}_2(\text{a})$] and rutile TiO_2 [$\text{TiO}_2(\text{r})$] expose $\text{Ti}-\text{O}$ site pairs consisting of five-coordinate Ti ($\text{Ti}_{5\text{c}}$) and two-coordinate O ($\text{O}_{2\text{c}}$) that differ significantly in acid and base strength between these crystalline phases. $\text{Ti}_{5\text{c}}$ centers in $\text{TiO}_2(\text{r})(110)$, the facet preferentially exposed in rutile,²¹ are much stronger Lewis acids than those in $\text{TiO}_2(\text{a})(101)$, the most abundant facet in anatase,²² as evident from their OH^- binding affinities [derived from density functional theory (DFT)] that are much more negative on $\text{TiO}_2(\text{r})(110)$ (-369 kJ mol^{-1}) than $\text{TiO}_2(\text{a})(101)$ (-246 kJ mol^{-1}).²³ In contrast, the $\text{O}_{2\text{c}}$ atoms in $\text{TiO}_2(\text{r})(110)$ are weaker Lewis bases, as shown by DFT-derived H^+ affinities that are less negative on $\text{TiO}_2(\text{r})(110)$ than on $\text{TiO}_2(\text{a})(101)$ (-1093 vs $-1175 \text{ kJ mol}^{-1}$, respectively).²³

In this study, HCOOH dehydration turnover rates and kinetic behaviors are compared on $\text{TiO}_2(\text{a})$ and $\text{TiO}_2(\text{r})$ powders at conditions that lead to sub-monolayer $^*\text{HCOO}^*$ coverages, thus ensuring access of $\text{Ti}_{5\text{c}}-\text{O}_{2\text{c}}$ pairs for HCOOH dehydration turnovers (513–563 K; 0.03–3 kPa HCOOH). The low coverages at such surfaces were confirmed by infrared spectra and product evolution rates from HCOOH -derived pre-adsorbed species. Kinetic and isotopic methods, together with DFT-derived energies of bound intermediates and transition states (TS), indicate that the kinetically relevant step involves TS in which the $\text{C}-\text{O}$ and $\text{C}-\text{H}$ bonds in molecularly bound HCOOH (HCOOH^*) are nearly cleaved, in processes that involve concerted interactions with the acid and the base centers in $\text{Ti}_{5\text{c}}-\text{O}_{2\text{c}}$ pairs. Such concerted interactions at the TS, taken together with its late character, make H_2O dissociation energies at a given $\text{Ti}_{5\text{c}}-\text{O}_{2\text{c}}$ pair a more accurate descriptor of HCOOH dehydration reactivity than the independent binding properties of each Lewis center at $\text{Ti}_{5\text{c}}-\text{O}_{2\text{c}}$ pairs. H_2O dissociation energies are similar at $\text{Ti}_{5\text{c}}-\text{O}_{2\text{c}}$ pairs on $\text{TiO}_2(\text{a})(101)$ and $\text{TiO}_2(\text{r})(110)$ surfaces because the stronger $\text{Ti}_{5\text{c}}$ Lewis acid centers in $\text{TiO}_2(\text{r})(110)$ compensate almost fully for the weaker $\text{O}_{2\text{c}}$ basic centers. This compensation leads to activation barriers for the first-order HCOOH dehydration rate constants that are similar on both TiO_2 surfaces, in spite of their very different acid and base strengths. These results also remind us about the risks in using

“simple” reactions as probes of surface properties without the unequivocal elucidation of the identity of the elementary steps and their kinetic consequences and the assessment of the number and type of the binding sites.

Such HCOOH dehydration routes, involving bare TiO_2 surfaces and a single kinetically relevant step, meet the requirements^{24,25} for applying microscopic reversibility tenets to the full catalytic sequence (instead of only to each elementary step). Consequently, the measured HCOOH dehydration rates and the gaseous thermodynamics of HCOOH dehydration, taken together, allow rigorous estimates of the rate of $\text{CO}-\text{H}_2\text{O}$ conversion to HCOOH . These HCOOH formation pathways may be relevant to the effects of oxide promoters in WGS but cannot be measured directly at WGS conditions because of unfavorable thermodynamics and the fast scavenging of HCOOH by a dehydrogenation function that completes WGS turnovers.

2. METHODS

2.1. Catalyst Preparation and Characterization.

$\text{TiO}_2(\text{a})$ (Sigma-Aldrich; 99.7%; $55 \text{ m}^2 \text{ g}^{-1}$; 32 nm) and $\text{TiO}_2(\text{r})$ (Sigma-Aldrich; 99.5%; $33 \text{ m}^2 \text{ g}^{-1}$; <100 nm) were treated in flowing dry air ($1.67 \text{ cm}^3 \text{ s}^{-1}$; Praxair; 99.999%) at 723 K for 15 h. These samples were then pressed into pellets, ground, and sieved to retain aggregates with different diameters (≤ 45 , ≤ 63 , 63–125, 125–180, and $\geq 425 \mu\text{m}$ in diameter). These aggregates were used to detect any kinetic consequences of intraparticle HCOOH concentration gradients.

The phase purity of TiO_2 powders before and after thermal treatment in air was confirmed by X-ray diffraction.¹³ Their surface areas were measured from N_2 uptakes at its normal boiling point using the Brunauer–Emmett–Teller formalism.²⁶ The measured surface areas were used together with the theoretical density of $\text{Ti}_{5\text{c}}-\text{O}_{2\text{c}}$ pairs in $\text{TiO}_2(\text{a})(101)$ and $\text{TiO}_2(\text{r})(110)$ surfaces estimated from their crystallographic structures ($5.2 \text{ Ti}_{5\text{c}}-\text{O}_{2\text{c}}$ pairs nm^{-2}) to calculate dehydration turnover rates by normalizing the measured rates by the number of $\text{Ti}_{5\text{c}}-\text{O}_{2\text{c}}$ pairs. The estimated site densities of $\text{Ti}_{5\text{c}}-\text{O}_{2\text{c}}$ pairs in TiO_2 samples were confirmed from the number of CO molecules evolved from $^*\text{HCOO}^*$ decomposition and the expected stoichiometry of one $^*\text{HCOO}^*$ moiety interacting with two $\text{Ti}_{5\text{c}}-\text{O}_{2\text{c}}$ pairs (Section 3.1). These $\text{Ti}_{5\text{c}}-\text{O}_{2\text{c}}$ densities are also consistent with the previous results using titrations with propionic acid.²³

2.2. HCOOH Dehydration Rate Measurements.

HCOOH dehydration rates were measured on TiO_2 powders held within a U-shaped quartz reactor (4 mm inner diameter). TiO_2 (0.001–0.03 g) was diluted with quartz powder (0.4 g; Sigma-Aldrich) to ensure plug-flow hydrodynamics and to avoid temperature nonuniformities along the catalyst bed. These quartz powders were treated with 1 M HNO_3 ($10 \text{ cm}^3 \text{ g}^{-1} \text{ SiO}_2^{-1}$), rinsed with deionized water (doubly-distilled; $\geq 17.6 \text{ M}\Omega\text{-cm}$ resistance), and dried in flowing dry air ($0.83 \text{ cm}^3 \text{ g}^{-1} \text{ s}^{-1}$; Praxair; 99.999%) at 373 K for 12 h. The empty reactor and these quartz powders did not show any detectable HCOOH decomposition products at the conditions used here for TiO_2 samples.

Temperatures were maintained using a resistively heated furnace and an electronic controller (Watlow, Series 982). A K-type thermocouple (Omega) located at the bed mid-point was used to monitor temperatures. Physical mixtures of TiO_2 and quartz sand were treated in flowing He ($1.67 \text{ cm}^3 \text{ s}^{-1}$;

Praxair; 99.999%) at 533 K for at least 0.5 h before the reaction. HCOOH (Sigma-Aldrich; $\geq 98\%$) and its isotopologues (DCOOH and DCOOD; Cambridge Isotope Laboratories; $\geq 98\%$ chemical and isotopic purities) were introduced as liquids without further purification into flowing He at 323 K using a syringe pump (KD Scientific, LEGATO 100). H₂O (doubly distilled, ≥ 17.6 M Ω -cm resistance) was also injected as a liquid using a separate syringe pump and vaporized at the injection port (at 373 K). All transfer lines were kept at ambient temperature except near the injection ports in order to prevent HCOOH decomposition on heated stainless-steel lines. HCOOH and H₂O pressures were kept well below their respective vapor pressures at 298 K (5.3 and 3.2 kPa,^{27,28} respectively) to avoid condensation within transfer lines. He (Praxair; 99.999%), CO (Praxair; 90% balance in Ar), O₂ (Praxair; dry air; 99.999%), and H₂ (Praxair; 99.95%) were metered so as to set the desired molar rates and reactant concentrations using electronic mass flow controllers (Porter, model 201). The concentrations of reactant and product streams were measured using on-line gas chromatography (Agilent, 6890A) with a packed column (Agilent Porapak-Q, 4.8 m, 80–100 mesh) and a thermal conductivity detector. Retention times and response factors were determined by injecting standards of known concentrations.

Possible corruptions of rate data by intraparticle HCOOH gradients were ruled out by HCOOH decomposition rates that did not depend on the aggregate size for particles smaller than 63–125 μm in diameter (Figure S1; Supporting Information); all reported kinetic data were measured on aggregates smaller than 45 μm in diameter. The effects of HCOOH depletion and of inhibition of rates by H₂O were taken into account using integral treatments for the analysis of rates in plug-flow systems (Section S6; Supporting Information); all reported rates represent those determined using these integral treatments at the concentrations of the inlet stream.

2.3. Temperature-Programmed Desorption and Surface Reaction (TPD/TPSR) of Pre-adsorbed HCOOH-Derived Species. Temperature-programmed desorption and surface reaction (TPD/TPSR) experiments were carried out on TiO₂ powders (0.45–0.75 g) held within the U-shaped quartz reactor described above. HCOOH-derived species were formed by exposing samples to 0.5 kPa HCOOH at ambient temperature. The temperature was then increased to 673 K (at 0.33 K s⁻¹) in flowing He, while HCOOH and CO concentrations in the effluent stream were measured continuously using an online infrared gas analyzer (MKS, MultiGas Series 2000).

The same procedure was used to measure in situ infrared spectra in transmission mode [Thermo Nicolet; Nexus 670; Hg–Cd–Te (MCT) detector]. Thin TiO₂ wafers (~ 10 mg cm⁻²) prepared by pressing powder samples were placed between KBr windows within a quartz cell. Spectra (2 cm⁻¹ resolution, 1 scan, 4000–650 cm⁻¹) were collected consecutively to give temporal information during temperature ramping. Rotational bands within the obtained spectra were removed using a low-pass parabolic filter (a pass frequency of 0 Hz and a stop frequency of 0.03 Hz).

2.4. UV–Visible Spectroscopy. UV–visible spectra were collected on TiO₂(r) samples using a spectrometer (Varian-Cary 6000) equipped with a Harrick Scientific diffuse reflectance accessory (DRP-XXX) and a reactor chamber (DRA-2CR). TiO₂(r) samples were treated in O₂ (20 kPa; 723

K; 15 h) or in H₂ (20 kPa; 823 K; 1 h) using the U-shaped reactor described above. These treated samples were loaded inside the reactor chamber and further treated in flowing He (433 K) for at least 0.5 h prior to the UV–vis measurements in flowing He at 433 K. In situ spectra were collected on H₂-treated samples during HCOOH dehydration (1.5 kPa HCOOH; 533 K) and during oxidation reactions (20 kPa O₂; 573 K). All gases and HCOOH reactants were delivered to a reactor chamber as described above. Temperatures were controlled by a temperature controller (Watlow, Series 982) and measured by a K-type thermocouple (Omega) placed at the wall of the sample holder. All spectra were collected between 0.5 and 3.5 eV at a scanning rate of 10 nm s⁻¹. The Kubelka–Munk function, $F(R_\infty)$ ($R_\infty = R_{\text{sample}}/R_{\text{reference}}$),²⁹ was used to convert the reflectance data into absorption spectra using MgO as the reference reflector.

2.5. Assessment of Elementary Steps and Bound Species by DFT and Statistical Mechanics Methods.

Periodic DFT methods were used to calculate the energies of all intermediates and TS involved in HCOOH dehydration elementary steps on TiO₂(a) (101) and TiO₂(r)(110) surfaces. The Perdew–Burke–Ernzerhof (PBE) functional³⁰ within the generalized gradient approximation was used to describe the electron exchange correlation as implemented in the Vienna Ab initio Simulation Package (VASP).^{31–33} The plane-wave basis sets were constructed using an energy cutoff of 396 eV with core electrons treated using projector-augmented wave methods.³⁴ Grimme's D2 methods³⁵ were used to describe van der Waals interaction energies, which are essential to describe adsorbate–adsorbate and adsorbate–surface interactions for weakly bound species. A Monkhorst–Pack grid of 8 \times 8 \times 8 was used for bulk calculations and a 4 \times 4 \times 1 grid was used for all slab models. Electronic structures were optimized until energy differences between successive iteration steps were $< 1 \times 10^{-6}$ eV and the atomic positions were optimized until the forces on all atoms were < 0.05 eV \AA^{-1} .

The lattice parameters of TiO₂(a) ($a = b = 0.379$, $c = 0.952$ nm) and TiO₂(r) ($a = b = 0.457$, $c = 0.296$ nm) were optimized using their known crystallographic structures as starting points [tetragonal, $I4_1/amd$, $a = b = 0.373$, $c = 0.937$ nm for TiO₂(a) and tetragonal, $P4_2/mnm$, $a = b = 0.459$, $c = 0.295$ nm for TiO₂(r)]²¹ and the methods described above. These optimized bulk structures were then used to construct the slab models of TiO₂(a)(101) and TiO₂(r)(110) surfaces, which represent the most prevalent facets for TiO₂(a)²² and TiO₂(r).²¹ Each slab consists of two Ti–O layers along with a 1.5 nm vacuum layer in between the slabs in the z -direction; HCOOH adsorption energy differed by only 1 kJ mol⁻¹ with slabs consisting of two or four Ti–O layers.¹³ The top TiO₂ layer and all bound species were fully relaxed in all calculations, while the atoms in the bottom layer were kept at their bulk atomic positions. (2 \times 2) and (2 \times 4) supercells (8 and 16 Ti–O pairs per layer) were used with one or two HCOOH molecules per supercell to model 1/4 and 1/8 ML coverages; only Ti_{5c}–O_{2c} pairs are used to define fractional occupancies because coordinatively saturated Ti_{6c} centers did not bind any intermediates or TS structures, as shown by their nearly zero DFT-derived OH⁻(g) affinities that are in sharp contrast with very large and negative values for Ti_{5c} centers on TiO₂(r)(110) (-369 kJ mol⁻¹) and TiO₂(a)(101) (-246 kJ mol⁻¹).²³

Adsorbate–adsorbate interactions are weak on TiO₂(a)-(101), as evidenced by the DFT-derived energy of formation

of $^*\text{HCOO}^*$ from $\text{HCOOH}(\text{g})$ that differs by less than 1 kJ mol^{-1} at $1/4$ and $1/8 \text{ ML } ^*\text{HCOO}^*$ coverages (-133 kJ mol^{-1} , electronic energies in Table S3, Supporting Information). This allowed energies of intermediates and TS on $\text{TiO}_2(\text{a})(101)$ to be accurately determined at $1/4 \text{ ML}$. Therefore, a (2×2) supercell of the $\text{TiO}_2(\text{a})(101)$ slab was used with one HCOOH molecule ($1/4 \text{ ML}$) in all calculations in order to limit the computational intensity. In contrast to such weak intermolecular interactions on $\text{TiO}_2(\text{a})(101)$, the shorter $\text{Ti}_{5c}-\text{Ti}_{5c}$ distances in $\text{TiO}_2(\text{r})(110)$ cause detectable repulsion among co-adsorbed $^*\text{HCOO}^*$ species [$\text{Ti}_{5c}-\text{Ti}_{5c} = 0.296$ vs 0.379 nm for $\text{TiO}_2(\text{r})(110)$ and $\text{TiO}_2(\text{a})(101)$, respectively]; $^*\text{HCOO}^*$ formation energies became less negative from -151 to -142 kJ mol^{-1} as $^*\text{HCOO}^*$ coverages increased from $1/8$ to $1/4 \text{ ML}$ (electronic energies, Table S3, Supporting Information). Consequently, a large (2×4) supercell of the $\text{TiO}_2(\text{r})(110)$ slab was used with one HCOOH molecule per supercell ($1/8 \text{ ML}$) in all calculations involving $\text{Ti}_{5c}-\text{O}_{2c}$ site pairs on rutile surfaces in order to avoid any artifacts associated with intercell interactions.

Kinetic relevance of defects in HCOOH dehydration was assessed by calculating energies of intermediates and TS on surface O-vacancies. These O-vacancies were modeled by removing one of the bridging O-atoms in the (2×2) supercell of the $\text{TiO}_2(\text{r})(110)$ slab (the geometry in Figure S5a; Supporting Information). One HCOOH or H_2O molecule was used with this slab containing an O-vacancy to calculate their binding energies. All calculations involving surface O-vacancies were performed with spin-polarization.

The minimum energy paths connecting the reactant, intermediate, and product states were calculated for each elementary step using nudged elastic band (NEB) methods³⁶ with an energy convergence criteria of $1 \times 10^{-4} \text{ eV}$ and a force criteria of 0.3 eV \AA^{-1} for all atoms. The structures located at the maximum energy point along the reaction coordinate (derived from NEB calculations) were used as the initial guesses for refinements of TS structures using Henkelman's dimer method³⁷ with convergence criteria of $1 \times 10^{-6} \text{ eV}$ for electronic energy and 0.05 eV \AA^{-1} for forces.

The vibrational frequencies of each structure were obtained using VASP and used to calculate zero-point vibrational energies (ZPVEs) and vibrational enthalpies and free energies at relevant temperatures using statistical mechanical formalisms.³⁸ The low-frequency vibrational modes, the strongest contributors to entropies, cannot be accurately described using harmonic oscillator models. They represent frustrated translational and rotational modes that are unrestricted in gaseous precursors but not in bound species. Hence, their contributions to vibrational entropies were replaced by a fraction (0.7) of the entropy of the respective molecules in a gas phase, as indicated by the measured adsorption entropies of weakly bound species on well-defined oxide surfaces.³⁹ These ZPVE and thermal contributions to enthalpies and free energies from vibrational modes (and translational and rotational modes for gas-phase molecules) were added to the dispersion-corrected DFT-derived electronic energies to give enthalpies and free energies of intermediates and TS at relevant reaction temperatures; all free energies are calculated at standard pressure (1 bar).

3. RESULTS AND DISCUSSION

3.1. Identity of Reactive Intermediates and Spectator Species and Their Surface Coverages from Infrared

Spectra and Desorption-Reaction Data. 3.1.1. Evidence for Bound HCOOH -Derived Species on Anatase TiO_2 . Figure 1a shows the infrared spectra of $\text{TiO}_2(\text{a})$ after exposure to 0.5

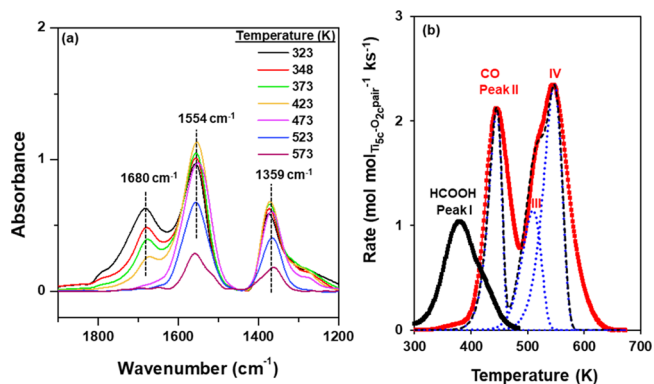


Figure 1. (a) Infrared spectra of $\text{TiO}_2(\text{a})$ measured in flowing He upon heating the sample (323–573 K) pre-exposed to 0.5 kPa HCOOH at ambient temperature. The spectra of $\text{TiO}_2(\text{a})$ were taken as the reference. (b) TPD of HCOOH pre-adsorbed on $\text{TiO}_2(\text{a})$ in flowing He (300–673 K). HCOOH evolution rates are shown in black squares and CO rates are shown in red squares. The CO peaks are deconvoluted assuming first-order decomposition, as shown as blue-dotted curves (deconvolution details in Section S2; Supporting Information); the black-dashed curve represents the combined contribution of the three blue-dotted curves.

kPa HCOOH at ambient temperature and heating to 573 K in flowing He. The strong bands at 1554 and 1359 cm^{-1} are assigned to antisymmetric and symmetric COO stretches in bidentate formates ($^*\text{HCOO}^*$) bound to vicinal Ti_{5c} centers on the basis of DFT-derived vibrational frequencies.^{13,40} The preferential formation of $^*\text{HCOO}^*$ and a co-adsorbed proton from $\text{HCOOH}(\text{g})$ on $\text{TiO}_2(\text{a})$ surfaces is consistent with its formation free energy from $\text{HCOOH}(\text{g})$ on $\text{TiO}_2(\text{a})(101)$ derived from dispersion-corrected DFT methods (PBE-D2) (-57 kJ mol^{-1} ; 433 K and 1 bar HCOOH) that is more negative than the formation of a Ti_{5c} -bound molecular HCOOH via its O atom in the $\text{C}=\text{O}$ group (-47 kJ mol^{-1} ; 433 K and 1 bar HCOOH).¹³ These conclusions contradict previous DFT results that suggested a Ti_{5c} -bound molecular HCOOH (via its $\text{C}=\text{O}$ group) as the most stable bound structure on $\text{TiO}_2(\text{a})(101)$ ^{41,42} because these calculations excluded dispersion corrections. More recent work based on first-principles molecular dynamic simulations⁴³ proposed that the H-atom in the OH group of Ti_{5c} -bound HCOOH (via its $\text{C}=\text{O}$ group) is shared between COO and a surface oxygen atom, forming a short strong hydrogen bond. This adsorption geometry, however, is inconsistent with the observed OH vibration mode (at 3655 cm^{-1}) in infrared spectra measured upon exposure of $\text{TiO}_2(\text{a})$ to 1.5 kPa HCOOH at 433 K and the subsequent desorption of weakly bound HCOOH species interacting with protons;¹³ such an OH band, taken together with co-existing COO stretching modes of $^*\text{HCOO}^*$ (at 1554 and 1359 cm^{-1}), indicates the dissociative adsorption of HCOOH on $\text{TiO}_2(\text{a})$ that forms $^*\text{HCOO}^*$ and a co-adsorbed proton. The adsorption mode of $^*\text{HCOO}^*$ at two Ti_{5c} centers also agrees with the number of CO molecules ($\text{CO}/\text{Ti}_{5c} = 0.45$) evolved upon decomposing such species on $\text{TiO}_2(\text{a})$ surfaces via thermal treatments, which is discussed next.

The additional band at 1680 cm^{-1} , as shown in Figure 1a, corresponds to $\text{C}=\text{O}$ stretches in molecularly bound

HCOOH;¹³ the shift of the C=O band in HCOOH(g) from 1757 to 1680 cm⁻¹ for bound HCOOH molecules reflects strong interactions of its O-atom in the C=O moiety with the protons at O_{2c} centers (HCOOH–H*) formed upon dissociation of HCOOH to *HCOO* species. The 1680 cm⁻¹ band weakens as the temperature increases and becomes undetectable above 473 K, indicative of removal of HCOOH–H* species by desorption or reaction at such temperatures. In contrast, the bands for *HCOO* (at 1554 and 1359 cm⁻¹; Figure 1a) remained essentially unchanged below 473 K and weakened only at higher temperatures. The very different temperatures required for the removal of bound HCOOH–H* and *HCOO* species, in turn, allow their respective amounts to be independently determined from the number of CO and HCOOH molecules evolved as the temperature increases.

The product evolution profiles contain four distinct features on TiO₂(a), one associated with HCOOH desorption and three with CO evolution (Figure 1b). The latter three features were deconvoluted using treatments for the first-order reactions of the bound species (details in Section S2; Supporting Information) in order to assess their respective contributions to the amount of CO formed. These three deconvoluted evolution features are shown as blue-dotted curves in Figure 1b; their combined contributions are shown as the black-dashed curve in Figure 1b, which accurately describes the measured CO evolution patterns.

The HCOOH peak and the first of the three CO evolution features (at <473 K; peaks I and II in Figure 1b) correspond to the desorption and decomposition of HCOOH–H* species, bound via interactions with protons formed upon HCOOH dissociation that forms the refractory *HCOO* template, a conclusion confirmed by the concurrent weakening of its infrared band in this temperature range. The CO evolution peaks at higher temperatures (>473 K; peaks III and IV in Figure 1b) reflect the decomposition of *HCOO* species, whose infrared bands (at 1554 and 1359 cm⁻¹) decrease only above 473 K, well after the HCOOH–H* band (at 1680 cm⁻¹) becomes undetectable (Figure 1a). The number of CO molecules evolved in features III and IV corresponds to a *HCOO*/(Ti_{5c}–O_{2c}) ratio of 0.45, in agreement with the expected binding stoichiometry for *HCOO* species bound at two Ti_{5c} centers. These results, in turn, indicate that Ti_{5c} centers in TiO₂(a) surfaces are saturated with *HCOO* species that remain intact below 473 K, thus preventing access to Ti_{5c}–O_{2c} pairs by any HCOOH molecules that decompose below such temperatures.

3.1.2. Evidence for Bound HCOOH-Derived Species on Rutile TiO₂. Figure 2a shows the infrared spectra of TiO₂(r) collected during heating of TiO₂(r) samples exposed to 0.5 kPa HCOOH at an ambient temperature. As on TiO₂(a), the weak band at 1680 cm⁻¹ for HCOOH–H* starts to weaken at 323 K and becomes undetectable above 523 K, a slightly higher temperature than on TiO₂(a) (473 K; Figure 1a). The bands for *HCOO* (at 1541 and 1370 cm⁻¹) remain unaffected below 523 K; these bands start to weaken at 523 K, a higher temperature than on TiO₂(a) (473 K; Figure 1a), indicative of the less reactive nature of *HCOO* species on TiO₂(r) than on TiO₂(a). The number of CO molecules that evolved from *HCOO* decomposition (>523 K; features III and IV in Figure 2b) corresponds to a *HCOO*/Ti_{5c}–O_{2c} ratio of 0.50, consistent with the saturation of Ti_{5c} centers with inactive *HCOO* species at temperatures below 523 K.

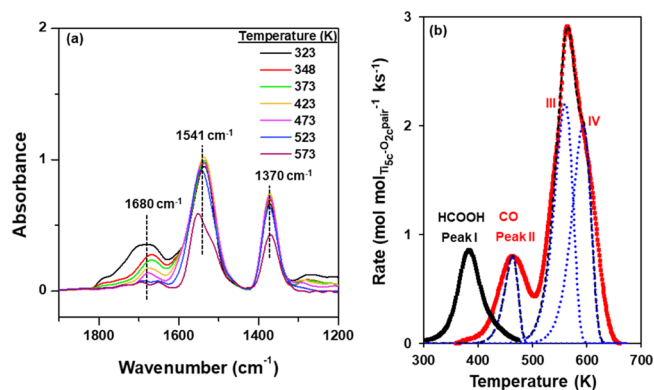


Figure 2. (a) Infrared spectra of TiO₂(r) measured in flowing He upon heating the sample (323–573 K) pre-exposed to 0.5 kPa HCOOH at ambient temperatures. The spectra of TiO₂(r) were taken as the reference. (b) TPD of HCOOH pre-adsorbed on TiO₂(r) in flowing He (300–673 K). HCOOH evolution rates are shown in black squares and CO rates are shown in red squares. The CO peaks are deconvoluted assuming first-order decomposition, shown as blue-dotted curves (deconvolution details in Section S2; Supporting Information); the black-dashed curve represents the combined contribution of the three blue-dotted curves.

3.1.3. State of TiO₂ Surfaces at Conditions of HCOOH Dehydration Catalysis. These infrared spectra and desorption reaction data show that Ti_{5c}–O_{2c} pairs at TiO₂(a) and TiO₂(r) surfaces remain saturated with strongly bound *HCOO* species that do not react at low temperatures (below 473–523 K). These *HCOO* species act by themselves as the template on top of which HCOOH dehydration turnovers occur. Consequently, the measured rates at these low temperatures reflect the reactivity of HCOOH–H* species bound at such refractory *HCOO* templates and only indirectly reflect the binding properties of Ti_{5c}–O_{2c} pairs; mechanistic details of HCOOH dehydration routes on *HCOO*-saturated TiO₂ surfaces were shown previously based on spectroscopic, kinetic, isotopic, and theoretical methods.¹³ These results, in turn, show that the intrinsic HCOOH dehydration reactivity of Ti_{5c}–O_{2c} pairs can be measured only when HCOOH dehydration turnovers occur at temperatures that allow the *HCOO* species to react.

3.2. Steady-State HCOOH Dehydration Turnover Rates and Kinetic Isotope Effects. Figure 3 shows HCOOH dehydration turnover rates (per Ti_{5c}–O_{2c} pair) on TiO₂(a) (513–553 K) and TiO₂(r) (533–563 K) crystalline powders as a function of HCOOH pressure (0.03–3 kPa); these temperatures and pressures lead to sub-monolayer *HCOO* coverages, thus ensuring access of Ti_{5c}–O_{2c} pairs by bound reactive intermediates. Neither CO₂ nor H₂ were detected as products at any conditions. HCOOH dehydration rates are initially proportional to HCOOH pressure at all temperatures and then increase sub-linearly at higher pressures (Figure 3), a transition that shifts to higher pressures with increasing temperature, as expected from higher *HCOO* coverages at higher HCOOH pressures and lower temperatures.

HCOOH dehydration rates were unaffected by the purposeful addition of CO to inlet streams, even at pressures much higher than those prevalent during HCOOH dehydration [0–4.5 kPa CO; 1 kPa HCOOH; 533 K; Figure S2a for TiO₂(a) and Figure S2b for TiO₂(r); Supporting Information]. These data show that CO does not compete

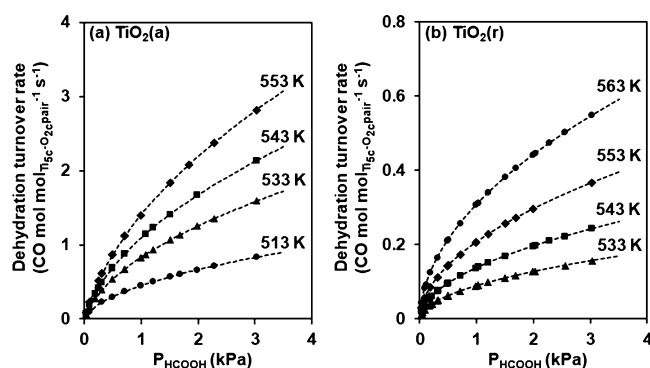


Figure 3. HCOOH dehydration turnover rates (per $\text{Ti}_{5c}\text{-O}_{2c}$ pair) on (a) $\text{TiO}_2(\text{a})$ (513–553 K) and (b) $\text{TiO}_2(\text{r})$ (533–563 K) as a function of HCOOH pressure (0.03–3 kPa). Reported rates were extrapolated to zero conversion using the integral form of eq 1 (details in Section S6; Supporting Information). Dashed curves represent the best regression fits of the rates to the functional form of eq 1.

with HCOOH-derived bound intermediates for $\text{Ti}_{5c}\text{-O}_{2c}$ pairs on $\text{TiO}_2(\text{a})$ or $\text{TiO}_2(\text{r})$. H_2O , the other HCOOH dehydration product, weakly inhibits HCOOH dehydration via competitive adsorption on $\text{Ti}_{5c}\text{-O}_{2c}$ site pairs [0–1.5 kPa H_2O ; 0.5 kPa HCOOH; 513–563 K; Figure S3a for $\text{TiO}_2(\text{a})$ and Figure S3b for $\text{TiO}_2(\text{r})$; Supporting Information]; such inhibition effects by H_2O were corrected using the integral treatments (Section S6; Supporting Information) and all reported rates represent those prevalent in the absence of any H_2O .

HCOOH dehydration rates on $\text{TiO}_2(\text{r})$ follow similar trends as on $\text{TiO}_2(\text{a})$ but are about tenfold smaller (Figure 3). The reactivity comparisons, however, become rigorous and accurate only when based on the individual kinetic parameters that account for such rates. These comparisons require, in turn, mechanistic interpretations of rates in terms of elementary steps and reactivity expressed in terms of kinetic and thermodynamic parameters.

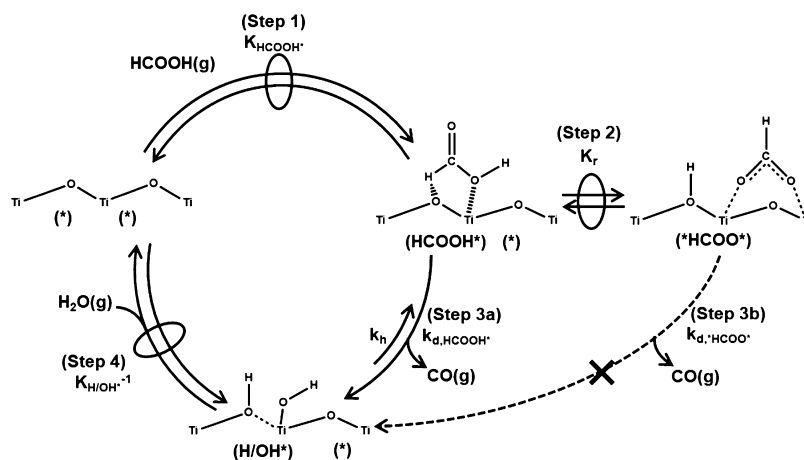
A plausible sequence of elementary steps for HCOOH dehydration is shown in Scheme 1. In this scheme, quasi-equilibrated adsorption of HCOOH on a $\text{Ti}_{5c}\text{-O}_{2c}$ pair forms molecularly bound HCOOH, interacting with a Ti_{5c} center via the O-atom in its OH group and with a O_{2c} center via the H-

atom at its CH group (HCOOH^* ; step 1; Scheme 1). This HCOOH^* intermediate can cleave its C–O and C–H bonds by reacting with a $\text{Ti}_{5c}\text{-O}_{2c}$ pair, forming CO as the incipient leaving group, as the O-atom in the OH group of HCOOH^* binds at the Ti_{5c} center and the vicinal O_{2c} abstracts the H-atom from its CH group (step 3a; Scheme 1). This pathway requires the concurrent involvement of the acid and base centers in $\text{Ti}_{5c}\text{-O}_{2c}$ pairs at the kinetically relevant step; it is reminiscent of E2 elimination pathways for alkanol dehydration at $\text{H}^+\text{-O}$ pairs in solid Brønsted acids, such as polyoxometalate clusters.⁴⁴ A HCOOH dehydration turnover is then completed by the quasi-equilibrated recombinative desorption of H_2O to re-form the $\text{Ti}_{5c}\text{-O}_{2c}$ pair (step 4; Scheme 1).

The cleavage of the O–H bond in HCOOH^* via H-abstraction by the O_{2c} center leads to the formation of a bidentate formate ($^*\text{HCOO}^*$) interacting with vicinal Ti_{5c} centers in a quasi-equilibrated step (step 2; Scheme 1). These $^*\text{HCOO}^*$ species (with co-adsorbed protons) represent the most stable form of the HCOOH-derived species at TiO_2 surfaces, as shown by the infrared spectra of the HCOOH-derived bound species during thermal treatments (Section 3.1). Such spectra show that $^*\text{HCOO}^*$ is the only bound species above 473 K on $\text{TiO}_2(\text{a})$ [and above 523 K on $\text{TiO}_2(\text{r})$]. $^*\text{HCOO}^*$ may cleave its C–O and C–H bonds to form a CO molecule via an intermolecular rearrangement in which the H-atom in its CH group is abstracted by the O-atom in $^*\text{HCOO}^*$ (step 3b; Scheme 1). This $^*\text{HCOO}^*$ -mediated CO formation route, however, shows very large DFT-derived free energy barriers ($\Delta G_{\text{d},^*\text{HCOO}^*}^{\ddagger} = +255 \text{ kJ mol}^{-1}$ from the $^*\text{HCOO}^*$ precursor on $\text{TiO}_2(\text{a})(101)$; 533 K; geometries shown in Figure S4; Supporting Information), making such routes kinetically inaccessible at these temperatures. This route is also inconsistent with the rate data because although measured rates can be approximately described by the rate equation predicted for these $^*\text{HCOO}^*$ -mediated pathways, the magnitudes and temperature dependences of the kinetic parameters are infeasible and contrary to expectations, as discussed below.

Both CO formation routes (via steps 3a or 3b; Scheme 1) involve concurrent C–O and C–H activation (in HCOOH^* or $^*\text{HCOO}^*$ intermediates). The involvement of the C–H

Scheme 1. Proposed Elementary Steps for HCOOH Dehydration on TiO_2 Surfaces^a



^aQuasi-equilibrated steps are denoted by oval symbols placed over double arrows. The nomenclature used for each bound species is shown inside the parenthesis below the structure.

bond at the kinetically relevant step is consistent with DCOOH dehydration rates that are about two-fold smaller than those of HCOOH, while DCOOH and DCOOD dehydration rates are similar (Figure 4; 533 K). The

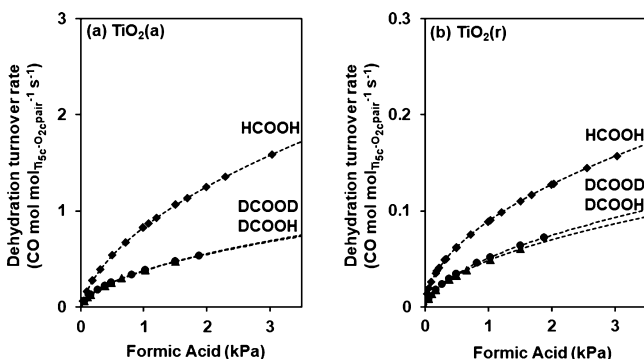


Figure 4. Dehydration turnover rates of HCOOH (◆), DCOOH (▲), and DCOOD (●) on (a) TiO₂(a) and (b) TiO₂(r) as a function of formic acid pressure (0.03–3 kPa; 533 K). Reported rates were extrapolated to zero conversion using the integral form of eq 1 (details in Section S6; Supporting Information). Dashed curves represent the best regression fits of the rates to the functional form of eq 1.

magnitudes of these isotope effects, however, need to be interpreted in terms of relevant rate parameters in order to provide mechanistic conclusions and rigorous comparisons to DFT-derived values, as we show below. Although both HCOOH*- and *HCOO*-mediated routes agree qualitatively with the observed kinetic isotope effects, they differ in the number of Ti_{5c}-O_{2c} site pairs that are required to bind the kinetically relevant TS; one Ti_{5c}-O_{2c} is required for the HCOOH*-mediated route (step 3a), while two vicinal Ti_{5c}-O_{2c} sites are required for the *HCOO*-mediated route (step 3b). As a result, they lead to rate equations with different functional forms and with different chemical origins for their respective regressed parameters.

HCOOH dehydration rates (per Ti_{5c}-O_{2c}; r_d) for the case of CO formation via the HCOOH* reaction at one Ti_{5c}-O_{2c} pair (step 3a; Scheme 1) are given by (derivation details in Section S5.1; Supporting Information)

$$r_d = \frac{2k_{d,HCOOH}K_{HCOOH}P_{HCOOH}}{1 + \sqrt{1 + 8K_{*HCOO}P_{HCOOH}}} = \frac{2k_{d,1}P_{HCOOH}}{1 + \sqrt{1 + 8K_{*HCOO}P_{HCOOH}}} \quad (1)$$

This equation reflects the elementary steps and parameters in Scheme 1 with an irreversible C–O and C–H activation elementary step (step 3a; Scheme 1). The denominator of eq 1 accounts for the relative number of unoccupied Ti_{5c}-O_{2c} pairs (*) and *HCOO* bound at two Ti_{5c}-O_{2c} pairs, which are the most abundant surface species. This rate equation accurately describes all the rate data on both TiO₂ surfaces, as shown by the dashed curves in Figure 3; the parity plots for TiO₂(a) and TiO₂(r) are shown in Figure S8 (Supporting Information).

The ($K_{*HCOO}P_{HCOOH}$) term in the denominator of eq 1 accounts for the sub-linear increase in the HCOOH dehydration rate as *HCOO* coverages increase with HCOOH pressure (Figure 3). K_{*HCOO} is the equilibrium constant for the formation of *HCOO* and a bound proton

from HCOOH(g) at two Ti_{5c}-O_{2c} pairs. It equals the combined $K_{HCOOH}K_r$ parameters for steps 1 and 2, as shown in Scheme 1, and reflects the free energy of formation of *HCOO* and a bound proton from HCOOH(g) at these two Ti_{5c}-O_{2c} pairs (ΔG_{*HCOO}^*). Its enthalpic and entropic components (ΔH_{*HCOO}^* and ΔS_{*HCOO}^*) are given by

$$K_{*HCOO}^* = \exp\left(\frac{-(G_{*HCOO}^* - G_{HCOOH(g)} - G_2^*)}{RT}\right) = \exp\left(\frac{-(\Delta H_{*HCOO}^* - T\Delta S_{*HCOO}^*)}{RT}\right) \quad (2)$$

Here, G_{*HCOO}^* and G_2^* represent the free energies of TiO₂ surfaces with and without a bound *HCOO* and a co-adsorbed proton; $G_{HCOOH(g)}$ is the free energy of gaseous HCOOH molecules.

The combined parameters ($k_{d,HCOOH}K_{HCOOH}^*$) in eq 1 represent the measured first-order rate constant ($k_{d,1} = k_{d,HCOOH}K_{HCOOH}^*$). These $k_{d,HCOOH}^*$ and K_{HCOOH}^* parameters cannot be separately measured because the K_{HCOOH}^* term in the numerator does not cancel out with the K_{*HCOO}^* term in the denominator as *HCOO* coverages approach saturation. The value of $k_{d,1}$ is determined by the Gibbs free energy of formation of the HCOOH* dehydration TS from HCOOH(g) and an unoccupied Ti_{5c}-O_{2c} pair ($\Delta G_{d,1}^\ddagger$; steps 1 and 3a; Scheme 1):

$$k_{d,1} = \frac{k_B T}{h} \exp\left(\frac{-(G_d^\ddagger - G_{HCOOH(g)} - G_*)}{RT}\right) = \frac{k_B T}{h} \exp\left(\frac{-(\Delta H_{d,1}^\ddagger - T\Delta S_{d,1}^\ddagger)}{RT}\right) \quad (3)$$

where k_B is the Boltzmann constant and h is the Planck's constant. These free energy, enthalpy, and entropy barriers ($\Delta G_{d,1}^\ddagger$, $\Delta H_{d,1}^\ddagger$ and $\Delta S_{d,1}^\ddagger$; eq 3) and the adsorption free energies, enthalpies, and entropies for *HCOO* (and a bound proton) formation from HCOOH(g) (ΔG_{*HCOO}^* , ΔH_{*HCOO}^* , and ΔS_{*HCOO}^* ; eq 2) were measured from a regression of the rate data at all temperatures (in Figure 3) to the functional forms of eqs 1–3 (regression details in Section S6; Supporting Information); these values are shown in Table 1 along with their respective uncertainty estimates.

On the bare Ti_{5c}-O_{2c} pairs prevalent at low HCOOH pressures, the rates are determined by the first-order rate constant ($k_{d,1}$; eq 1). The measured free energy barrier ($\Delta G_{d,1}^\ddagger$) that determines this $k_{d,1}$ constant (through eq 3) is only slightly larger on TiO₂(a) than TiO₂(r) ($+109 \pm 1$ and $+94 \pm 1$ kJ mol⁻¹, respectively; 533 K; Table 1). Their enthalpic barriers are also within experimental uncertainties [$+20 \pm 3$ kJ mol⁻¹ for TiO₂(a) and $+18 \pm 5$ kJ mol⁻¹ for TiO₂(r); Table 1]. These results, in turn, indicate that TiO₂(a) is slightly less reactive than TiO₂(r) when the surfaces are essentially bare because the first-order rate constants predominately account for measured rates in such instances.

As surfaces become increasingly covered with *HCOO* species, the rates increase sub-linearly with HCOOH pressure (Figure 3); such rates depend not only on the value of $k_{d,1}$ in the numerator of eq 1 but also on its denominator K_{*HCOO}^* term. The measured free energies for the formation of *HCOO* and a bound proton from HCOOH(g), which account for the K_{*HCOO}^* term (via eq 2), are negative on both

Table 1. Corresponding Free Energy, Enthalpy, and Entropy for K_{*HCOO^*} and $k_{d,1}$ Parameters in Eq 1 from Experiment and Theory for $TiO_2(a)$ and $TiO_2(r)$

	$TiO_2(a)$		$TiO_2(r)$	
	exp ^a	theory ^b	exp ^a	theory ^b
	K_{*HCOO^*}			
ΔG_{*HCOO^*} (kJ mol ⁻¹) at 533 K	-25 ± 2	-42	-75 ± 1	-64
ΔH_{*HCOO^*} (kJ mol ⁻¹)	-109 ± 7	-128	-149 ± 7	-149
ΔS_{*HCOO^*} (J K ⁻¹ mol ⁻¹)	-158 ± 14	-161	-139 ± 13	-158
	$k_{d,1}$ (= $k_{d,HCOOH} K_{*HCOO^*}$)			
$\Delta G_{d,1}^\ddagger$ (kJ mol ⁻¹) at 533 K	+109 ± 1	+99	+94 ± 1	+94
$\Delta H_{d,1}^\ddagger$ (kJ mol ⁻¹)	+20 ± 3	+26	+18 ± 5	+25
$\Delta S_{d,1}^\ddagger$ (J K ⁻¹ mol ⁻¹)	-167 ± 6	-135	-142 ± 9	-130

^aUncertainties reflect 95% confidential intervals. Measured by fitting the rate data (in Figure 3) to the functional forms of eqs 1–3 (regression details in Section S6; Supporting Information). ^bFree energies are calculated at 533 K and standard pressure (1 bar).

$TiO_2(a)$ and $TiO_2(r)$ ($\Delta G_{*HCOO^*} = -25 \pm 2$ and -75 ± 1 kJ mol⁻¹, respectively; 533 K; Table 1), consistent with infrared and TPD/TPSR data (Section 3.1). ΔG_{*HCOO^*} values are more negative on $TiO_2(r)$ than on $TiO_2(a)$, as is also the case for their respective enthalpic components ($\Delta H_{*HCOO^*} = -109 \pm 7$ kJ mol⁻¹ on $TiO_2(a)$ and -149 ± 7 kJ mol⁻¹ on $TiO_2(r)$; Table 1), indicative of the stronger binding of $*HCOO^*$ on $TiO_2(r)$. A stronger $*HCOO^*$ binding, in turn, leads to significantly lower HCOOH dehydration rates on $TiO_2(r)$ at high HCOOH pressures (Figure 3) when surfaces reach near-saturation $*HCOO^*$ coverages because the strongly bound $*HCOO^*$ must either desorb for HCOOH(g) to access the $Ti_{5c}-O_{2c}$ pairs or be converted to HCOOH* in order to form CO products.

The above mechanistic interpretations, in terms of free energies and enthalpies for relevant elementary steps (in Scheme 1), allow the benchmarking of theory and experiment values; a comparison among measured and DFT-derived values is included in Table 1, and the detailed DFT calculations and findings are described in the next section. These theoretical treatments also allow quantitative assessments of kinetic isotopic effects (KIEs) based on rate and equilibrium constants (instead of just HCOOH dehydration rates). Measured KIE values, defined as the ratio of $k_{d,1}$ constants for HCOOH to that of each deuterium isotopologue, are determined from regressed $k_{d,1}$ constants for HCOOH, DCOOH, and DCOOD via eq 1; they are listed in Table 2 along with their respective uncertainties.

Table 2. KIEs for the First-Order Rate Constant, $k_{d,1}$ (Eq 1; 533 K) from Experiments and Theory for $TiO_2(a)$ and $TiO_2(r)$

	$TiO_2(a)$		$TiO_2(r)$	
	exp ^a	theory ^b	exp ^a	theory ^b
HCOOH/DCOOH	2.0 ± 0.1	2.0	1.8 ± 0.1	1.9
HCOOH/DCOOD	1.8 ± 0.1	1.6	1.5 ± 0.1	1.5

^aUncertainties reflect 95% confidence intervals. The $k_{d,1}$ values are estimated by regressing the rate data in Figure 4 to the functional form of eq 1. ^bDFT-derived rate constants are calculated from free energies at 533 K and standard pressure (1 bar) via eq 3.

The alternate $*HCOO^*$ -mediated route (step 3b; Scheme 1) involves two vicinal $Ti_{5c}-O_{2c}$ pairs in stabilizing the kinetically relevant C–O and C–H activation TS. For irreversible C–O/C–H activation (step 3b; Scheme 1) and bare $Ti_{5c}-O_{2c}$ pairs and $*HCOO^*$ as the most abundant surface species, HCOOH dehydration rates (per $Ti_{5c}-O_{2c}$; r_d) are given by (derivation details in Section S5.2; Supporting Information)

$$r_d = \frac{4k_{d,*HCOO^*}K_{*HCOO^*}P_{HCOOH}}{(1 + \sqrt{1 + 8K_{*HCOO^*}P_{HCOOH}})^2} \quad (4)$$

The $k_{d,*HCOO^*}$ parameter in the numerator is the first-order $*HCOO^*$ decomposition rate constant (step 3b; Scheme 1) and reflects the free energy of this dehydration TS references to its $*HCOO^*$ precursor ($\Delta G_{d,*HCOO^*}^\ddagger$)

$$k_{d,*HCOO^*} = \frac{k_B T}{h} \exp\left(\frac{-(G_{d,*HCOO^*}^\ddagger - G_{*HCOO^*})}{RT}\right) \\ = \frac{k_B T}{h} \exp\left(\frac{-(\Delta H_{d,*HCOO^*}^\ddagger - T\Delta S_{d,*HCOO^*}^\ddagger)}{RT}\right) \quad (5)$$

K_{*HCOO^*} is the equilibrium constant for the formation of $*HCOO^*$ and a bound proton from HCOOH(g) (steps 1 and 2; Scheme 1; eq 2); it appears in both the numerator and denominator of eq 4. The adsorption free energy, enthalpy, and entropy of the $*HCOO^*$ species (ΔG_{*HCOO^*} , ΔH_{*HCOO^*} and ΔS_{*HCOO^*} ; eq 2) and the free energy, enthalpy, and entropy barriers ($\Delta G_{d,*HCOO^*}^\ddagger$, $\Delta H_{d,*HCOO^*}^\ddagger$, and $\Delta S_{d,*HCOO^*}^\ddagger$; eq 5) are estimated by regressing the rate data (in Figure 3a) to the functional forms of eqs 2, 4, and 5; these values and their uncertainties are listed in Table 3.

Table 3. Corresponding Free Energy, Enthalpy, and Entropy of K_{*HCOO^*} and $k_{d,*HCOO^*}$ Parameters (in Eq 4) for $TiO_2(a)$

	$TiO_2(a)$	
	exp ^a	theory ^b
	K_{*HCOO^*}	
ΔG_{*HCOO^*} (kJ mol ⁻¹) at 533 K	-13 ± 1	-42
ΔH_{*HCOO^*} (kJ mol ⁻¹)	-23 ± 13	-128
ΔS_{*HCOO^*} (J K ⁻¹ mol ⁻¹)	-17 ± 26	-161
	$k_{d,*HCOO^*}$	
$\Delta G_{d,*HCOO^*}^\ddagger$ (kJ mol ⁻¹) at 533 K	+125 ± 1	+255
$\Delta H_{d,*HCOO^*}^\ddagger$ (kJ mol ⁻¹)	+78 ± 11	+287
$\Delta S_{d,*HCOO^*}^\ddagger$ (J K ⁻¹ mol ⁻¹)	-87 ± 20	+60

^aUncertainties reflect 95% confidential intervals. ^bThese values are estimated by fitting the rate data in Figure 3a to the functional forms of eqs 2, 4, and 5.

These estimated adsorption entropies ($\Delta S_{*HCOO^*} = -17 \pm 26$ J K⁻¹ mol⁻¹; Table 3) are inconsistent with the entropy losses expected upon the formation of $*HCOO^*$ from HCOOH(g) using statistical mechanical treatments (Section 2.5) and DFT-derived vibrational frequencies of $*HCOO^*$ and HCOOH(g) (-161 J K⁻¹ mol⁻¹; Table 3). Adsorption enthalpies ($\Delta H_{*HCOO^*} = -23 \pm 13$ kJ mol⁻¹; Table 3) are also inconsistent with the strong binding of $*HCOO^*$ on TiO_2 surfaces evident from infrared spectra and TPD/TPSR data (Section 3.1). The large uncertainties in these values reflect the

inadequacy of the functional form of eq 4 in describing the measured rate data. The activation entropy corresponding to the formation of the decomposition TS from $^*\text{HCOO}^*$ ($\Delta S_{\ddagger, \text{HCOO}^*}^\ddagger = -87 \pm 20 \text{ J K}^{-1} \text{ mol}^{-1}$; Table 3) is large and negative, inconsistent with the small and positive entropy changes expected upon the formation of the $^*\text{HCOO}^*$ decomposition TS, in which the CO molecule becomes more loosely bound to the decomposing moiety than in its strongly bound $^*\text{HCOO}^*$ precursor; the activation entropy expected from the DFT method is $+60 \text{ J K}^{-1} \text{ mol}^{-1}$ (Table 3). These inconsistencies, taken together with the inaccurate descriptions of rate data reflected in the parameter uncertainties for the $^*\text{HCOO}^*$ -mediated route (eq 4; step 3b; Scheme 1), indicate that such rate equations do not reflect the chemical origins of measured rates, even though they describe the general kinetic trends observed for HCOOH dehydration rates (parity plots; Figure S10; Supporting Information).

These strongly bound $^*\text{HCOO}^*$ species decompose instead to CO and H_2O by re-forming their weakly bound HCOOH* precursors, which then cleave their C–O and C–H bonds via interactions with the acid and base centers in $\text{Ti}_{5c}-\text{O}_{2c}$ pairs (steps 2 and 3a; Scheme 1). In effect, strongly bound species must “climb up” in energy and re-cross the “ledge” from which they are formed along the reaction coordinate in order to lead up to the TS, where a smaller barrier decomposes it into CO products, all without overcoming the large barrier associated with its direct decomposition. These conclusions are consistent with DFT-derived energies of intermediates and TS on $\text{TiO}_2(\text{a})$ and $\text{TiO}_2(\text{r})$ surfaces, which are discussed next.

3.3. Theoretical Assessments of HCOOH Dehydration Elementary Steps on TiO_2 Surfaces and the Effects of Their Acid–Base Properties on Catalytic Reactivity.

3.3.1. Energies of Intermediates and TS on $\text{TiO}_2(\text{a})(101)$ from DFT Methods. Figure 5 illustrates DFT-derived free energies of intermediates and TS involved in the HCOOH dehydration elementary steps, as depicted in Scheme 1, for $\text{TiO}_2(\text{a})(101)$ surfaces along with their molecular structures. HCOOH adsorption on a $\text{Ti}_{5c}-\text{O}_{2c}$ pair forms HCOOH* (Figure 5a; step 1; Scheme 1). The NEB path that connects a HCOOH(g) molecule with its bound HCOOH* form did not detect any energy barrier, consistent with the quasi-equilibrated nature of this molecular adsorption step. The DFT-derived free energy of formation of HCOOH* from HCOOH(g) ($\Delta G_{\text{HCOOH}^*}^\ddagger$) determines the K_{HCOOH^*} constant (in eq 1) and is $+7 \text{ kJ mol}^{-1}$ (Figure 5a; 533 K; 1 bar HCOOH), which is consistent with the low HCOOH* coverages observed during HCOOH dehydration and with denominator terms in eq 1 that reflect only the coverage of strongly bound $^*\text{HCOO}^*$ species. This K_{HCOOH^*} value cannot be measured separately from steady-state measurements because of the functional form of eq 1, specifically because the K_{HCOOH^*} numerator term does not cancel the $K_{^*\text{HCOO}^*}$ denominator term at high $^*\text{HCOO}^*$ coverages, thus precluding independent estimation of K_{HCOOH^*} and $k_{\text{d},1}$. These reactive HCOOH* intermediates, therefore, exist only as a minority species, as also evident from infrared spectra that show the predominant presence of $^*\text{HCOO}^*$ as the bound species during catalysis (Section 3.1), but they provide the sole reactive route to CO and H_2O products.

The HCOOH* species cleave their C–O and C–H bonds through concerted interactions with a $\text{Ti}_{5c}-\text{O}_{2c}$ pair to form CO as the incipient leaving group (step 3a; Scheme 1). No

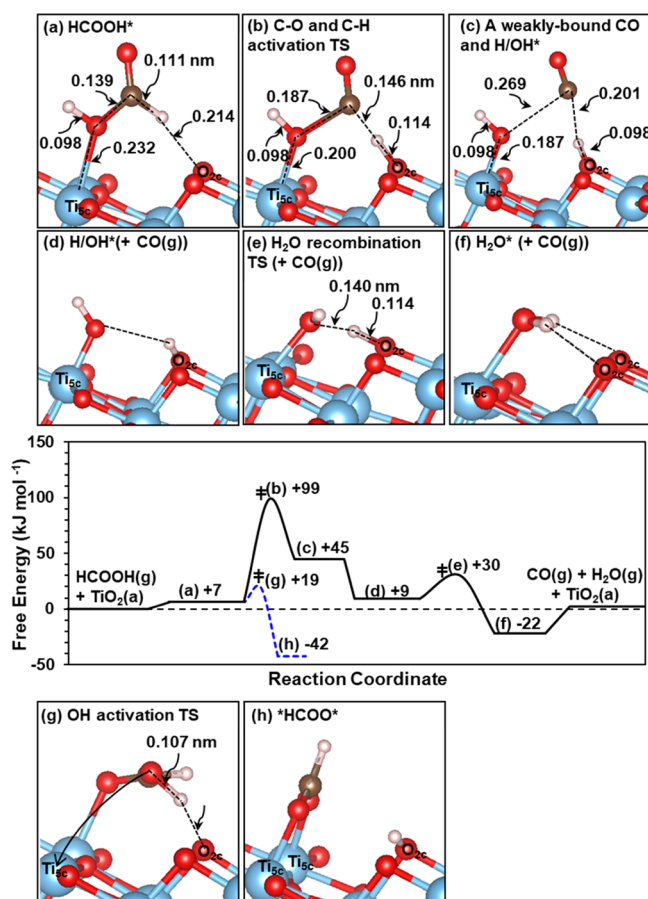


Figure 5. DFT-derived free energies (kJ mol^{-1} ; 533 K; 1 bar HCOOH) of intermediates and TS involved in HCOOH dehydration on $\text{TiO}_2(\text{a})(101)$ via elementary steps, as depicted in Scheme 1. The energies are referenced to HCOOH(g) and the surface. The corresponding geometries are also shown with bond distances (in nm).

sequential C–O and C–H activation routes were detected by NEB searches and all attempts at sequential routes converged instead to the concerted route. The TS that mediates such transformations (Figure 5b) imposes the highest free energy barrier along the HCOOH dehydration reaction coordinate, which is consistent with its role as the sole kinetically-relevant step.

The free energy of formation of this TS from HCOOH(g) ($\Delta G_{\text{d},1}^\ddagger$) determines the first-order dehydration rate constant, $k_{\text{d},1}$ (in eq 1), through eq 3. The DFT-derived free energy barrier for $\text{TiO}_2(\text{a})(101)$ ($\Delta G_{\text{d},1}^\ddagger = +99 \text{ kJ mol}^{-1}$; 533 K) agrees well with the measured values ($+109 \pm 1 \text{ kJ mol}^{-1}$; 533 K, Table 1), as is also the case for the respective enthalpy components ($\Delta H_{\text{d},1}^\ddagger = +26$ vs $+20 \pm 3 \text{ kJ mol}^{-1}$ from DFT and experiments, respectively; Table 1).

DFT-derived KIE values, given by the ratio of the $k_{\text{d},1}$ constants for HCOOH and each isotopologue, also agree with the measured values (Table 2). The DFT-derived KIE value for HCOOH/DCOOH on $\text{TiO}_2(\text{a})(101)$ is 2.0 at 533 K, in excellent agreement with experiments (2.0 ± 0.1 ; Table 2), as is also the case for HCOOH/DCOOD KIE values (1.6 from DFT vs 1.8 ± 0.1 from experiments; 533 K; Table 2). Such quantitative agreements between DFT-derived barriers and KIE and experimental values support the proposed chemical origins of the measured rate parameters and the identity and

kinetic relevance of the elementary steps in Scheme 1 for the HCOOH dehydration catalytic sequence.

The reaction free energy for this C–O and C–H activation step (step 3a, Scheme 1) is +38 kJ mol⁻¹ (Figure 5c). The bound CO molecule desorbs in an exergonic step (–36 kJ mol⁻¹), indicative of its loosely-bound character. The OH bound at the Ti_{5c} center and the H-atom bound at the O_{2c} center (H/OH*; Figure 5d) ultimately recombine to form a bound H₂O interacting with the Ti_{5c} center (H₂O*; Figure 5f) in an exergonic step (–31 kJ mol⁻¹); this step is quasi-equilibrated, as shown by the small free energy barrier required to form the TS (Figure 5e) that transfers the H-atom to the OH group (+21 kJ mol⁻¹). A HCOOH dehydration turnover is completed by the desorption of H₂O molecule in an endergonic step (+24 kJ mol⁻¹; step 4; Scheme 1).

Weakly bound HCOOH* species can also form *HCOO* bound at vicinal Ti_{5c} centers and a bound proton at an O_{2c} center (Figure 5h) in an exergonic step (–49 kJ mol⁻¹; 533 K; step 2; Scheme 1) that exhibits a very small free energy barrier for the activation of the O–H bond in HCOOH* by an O_{2c} center (+12 kJ mol⁻¹; 533 K; Figure 5g). The DFT-derived free energy for the formation of *HCOO* and a bound proton (Figure 5h) from HCOOH(g) at two Ti_{5c}–O_{2c} pairs (ΔG_{HCOO}^*) determines the K_{HCOO}^* constant in eq 1. This ΔG_{HCOO}^* value is large and negative (–42 kJ mol⁻¹; 533 K), which is consistent with *HCOO* (and a co-adsorbed proton) as the predominant species on TiO₂(a). Such ΔG_{HCOO}^* values and the corresponding enthalpies are more negative than the experimental values ($\Delta G_{\text{HCOO}}^* = -42$ vs -25 ± 2 kJ mol⁻¹ at 533 K and $\Delta H_{\text{HCOO}}^* = -128$ vs -109 ± 7 kJ mol⁻¹ from DFT and experiment, respectively; Table 1).

Reactive HCOOH* and unreactive *HCOO* species are in quasi-equilibrium because their interconversion barriers (via step 2; Scheme 1) are much smaller than for the decomposition of *HCOO* species (via step 3b; Scheme 1), as shown by DFT-derived free energies for the formation of the interconversion TS from *HCOO* precursors (+61 kJ mol⁻¹; 533 K; Figure 5g) that are much smaller than to form the *HCOO* decomposition TS from the same *HCOO* precursor ($\Delta G_{\text{d,HCOO}}^{\ddagger} = +255$ kJ mol⁻¹; 533 K; Figure S4 in Supporting Information). Consequently, the strongly bound *HCOO* leads to the CO product by re-forming its more weakly bound precursor, HCOOH* (step 2; Scheme 1), which provides a route to the CO products with much lower barriers (step 3a; Scheme 1) than from direct *HCOO* decomposition (step 3b; Scheme 1).

The kinetic irrelevance of direct *HCOO* decomposition routes (step 3b; Scheme 1) is also consistent with the large DFT-derived free energy barrier for the *HCOO* decomposition step ($\Delta G_{\text{d,HCOO}}^{\ddagger} = +255$ kJ mol⁻¹; 533 K; Figure S4 in Supporting Information), which is much larger than the measured value ($+125 \pm 1$ kJ mol⁻¹; 533 K; Table 3). These results, in turn, act as a reminder that the fit of the rate expression does not provide concrete evidence for reaction mechanisms unless accompanied by consistency checks of the regressed rate parameters for their chemical origins.

3.3.2. Energies of Intermediates and TS on TiO₂(r)(110) from DFT Methods. Figure 6 shows DFT-derived free energies and structures of intermediates and TS involved in HCOOH dehydration elementary steps (in Scheme 1) on TiO₂(r)(110). The free energy of HCOOH* formation from HCOOH(g) at a Ti_{5c}–O_{2c} pair on TiO₂(r)(110) ($\Delta G_{\text{HCOOH}^*}$; step 1; Scheme 1) is small and negative (–9 kJ mol⁻¹; Figure 6a; 533 K). This

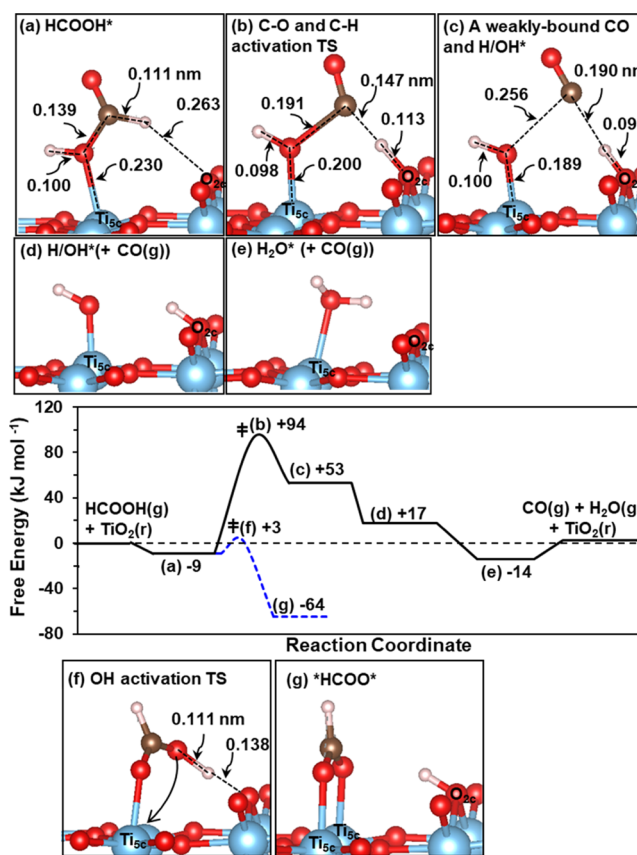


Figure 6. DFT-derived free energies (kJ mol⁻¹; 533 K; 1 bar HCOOH) of intermediates and TS involved in HCOOH dehydration on TiO₂(r)(110) via elementary steps as depicted in Scheme 1. The energies are referenced to HCOOH(g) and the surface. The corresponding geometries are also shown with bond distances (in nm).

step is slightly more favorable on TiO₂(r)(110) than on TiO₂(a)(101) ($\Delta G_{\text{HCOOH}^*} = -9$ vs $+7$ kJ mol⁻¹; Figures 5a and 6a; 533 K). The formation free energy of HCOOH* (from HCOOH(g)) at a Ti_{5c}–O_{2c} pair on TiO₂(r)(110) is much less negative than that for the formation of a *HCOO* and a bound proton from a HCOOH(g) molecule and two Ti_{5c}–O_{2c} pairs (–9 vs –64 kJ mol⁻¹; 533 K), consistent with infrared spectra and desorption reaction data, which show that the *HCOO* species (with co-adsorbed protons) are the predominant bound species on TiO₂(r) at the temperatures used in this study (Section 3.1).

The TS that mediates the kinetically relevant HCOOH* dehydration step (step 3a; Scheme 1; Figure 6b) imposes the highest barrier along the reaction coordinate. Its free energy of formation from HCOOH(g) ($\Delta G_{\text{d,1}}^{\ddagger}$) accounts for the magnitude of the first-order HCOOH dehydration rate constant, $k_{\text{d,1}}$ (in eq 1). DFT-derived $\Delta G_{\text{d,1}}^{\ddagger}$ values and their enthalpic components are in quantitative agreements with the measurements [$\Delta G_{\text{d,1}}^{\ddagger} = +94$ (DFT) vs $+94 \pm 1$ (exp.) kJ mol⁻¹ at 533 K and $\Delta H_{\text{d,1}}^{\ddagger} = +25$ (DFT) vs $+18 \pm 5$ (exp.) kJ mol⁻¹; Table 1]. The DFT-derived KIE values for HCOOH/DCCOOH on TiO₂(r)(110) is 1.9, while the measured value is 1.8 ± 0.1 (533 K; Table 2). The same HCOOH/DCCOOH values were obtained from the theory and experiment (1.5 ± 0.1 ; 533 K; Table 2).

The free energy of formation of a weakly bound CO and a dissociated H₂O molecule at a Ti_{5c}–O_{2c} pair from HCOOH*

(step 3a; Scheme 1) is +62 kJ mol⁻¹ (Figure 6c; 533 K). The CO formed desorbs in an exergonic step (-36 kJ mol⁻¹; Figure 6d; 533 K). The H/OH* at a Ti_{5c}-O_{2c} pair (Figure 6d) recombines to form H₂O* (Figure 6e); this step is exergonic (-31 kJ mol⁻¹; 533 K) and occurs without a detectable barrier. H₂O* desorbs in an endergonic step (+16 kJ mol⁻¹; step 4; Scheme 1).

HCOOH* also forms *HCOO* and a bound proton at two Ti_{5c}-O_{2c} pairs via the activation of its O-H (step 2; Scheme 1) in a step that is essentially barrierless (+12 kJ mol⁻¹; activation free energy; Figure 6f; 533 K). The formation free energy of this *HCOO* and the co-adsorbed proton from HCOOH(g) (ΔG_{HCOO^*}) determines the K_{HCOO^*} constant (in eq 1). Such a DFT-derived ΔG_{HCOO^*} value and its enthalpic component agree well with the experimental values ($\Delta G_{\text{HCOO}^*} = -64$ (DFT) vs -75 ± 1 (exp.) kJ mol⁻¹ at 533 K; $\Delta H_{\text{HCOO}^*} = -149$ (DFT) vs -149 ± 7 (exp.) kJ mol⁻¹; Table 1).

3.3.3. Acid-Base Properties of Ti_{5c}-O_{2c} Pairs and the Energetics of Intermediates and TS in HCOOH Dehydration Elementary Steps. HCOOH dehydration turnovers occur at Ti_{5c}-O_{2c} pairs on stoichiometric TiO₂(a)(101) and TiO₂(r)(110) surfaces, which expose Ti_{5c} and O_{2c} centers that differ significantly in their acid and base strengths, as shown by their respective DFT-derived OH⁻ and H⁺ affinities.²³ Ti_{5c} centers on TiO₂(r)(110) are stronger acids than on TiO₂(a)(101), evidenced by their much more negative OH⁻ affinities (-369 vs -246 kJ mol⁻¹).²³ In contrast, O_{2c} centers in TiO₂(r)(110) are weaker bases, as shown by DFT-derived H⁺ affinities that are less negative on TiO₂(r)(110) than on TiO₂(a)(101) (-1093 vs -1175 kJ mol⁻¹).²³ Yet, the activation barriers associated with the formation of the kinetically relevant TS from HCOOH(g) are similar on both TiO₂(a)(101) and TiO₂(r)(110) surfaces whether compared based on theory ($\Delta H_{\text{d},1}^{\ddagger} = +26$ vs +25 kJ mol⁻¹) or experiments ($\Delta H_{\text{d},1}^{\ddagger} = +20 \pm 3$ vs +18 ± 5 kJ mol⁻¹) (Table 1).

These kinetically relevant TS on TiO₂ surfaces occur late along the reaction coordinate of the HCOOH* dehydration step (step 3a; Scheme 1). The OH group in HCOOH* is nearly attached to the Ti_{5c} center and the (H)O-Ti_{5c} bond is nearly formed at the TS on TiO₂(a)(101) (0.200 nm; Figure 5b); the latter varies from 0.232 nm in the HCOOH* reactant (Figure 5a) to 0.187 nm at the product state (H/OH*; Figure 5c). Concurrently, the H-atom in the CH group of HCOOH* is almost fully transferred to the O_{2c} center in TiO₂ at the TS; the H-O_{2c} bond (0.114 nm; Figure 5b) is much shorter than in bound HCOOH* species (0.214 nm; Figure 5a) and similar to its 0.098 nm length in the H/OH* product (Figure 5c). Similar conclusions are evident on TiO₂(r)(110) surfaces, for which (H)O-Ti_{5c} and H-O_{2c} bonds at the TS (0.200 and 0.113 nm; Figure 6b) resemble those in the H/OH* product (0.189 and 0.098 nm; Figure 6c) but are much shorter than those in the HCOOH* reactants (0.230 and 0.263 nm; Figure 6a).

The structures of the relevant TS and their concerted interactions with the acid and base centers in Ti_{5c}-O_{2c} indicate that independent descriptors of the strength of these acid and base centers are not accurate proxies for the stability of such TS and, thus, for HCOOH dehydration turnover rates. The late character of these TS structures, evident from the nearly formed (H)O-Ti_{5c} and H-O_{2c} bonds, suggests that H₂O dissociation energies at a Ti_{5c}-O_{2c} pair on each TiO₂ surface may represent a more appropriate descriptor of the reactivity

of these Ti_{5c}-O_{2c} pairs as they stabilize the kinetically relevant TS in a concerted manner.

TiO₂(r)(110) contains Ti_{5c} centers that are stronger acids than those on TiO₂(a)(101) surfaces but with O_{2c} centers that are more weakly basic. These two effects, in fact, act in balance and lead to similar dissociative H₂O adsorption enthalpies at Ti_{5c}-O_{2c} pairs on TiO₂(a)(101) and TiO₂(r)(110) surfaces ($\Delta H_{\text{H/OH}^*} = -56$ vs -49 kJ mol⁻¹, respectively). Not surprisingly, their Ti_{5c}-O_{2c} pairs stabilize the TS to similar extents, leading to similar activation barriers as demonstrated by both theory ($\Delta H_{\text{d},1}^{\ddagger} = +26$ vs +25 kJ mol⁻¹) and experiments (+20 ± 3 vs +18 ± 5 kJ mol⁻¹; Table 1).

We conclude that such a compensation of acid and base strengths in Ti_{5c} and O_{2c} centers on TiO₂(a)(101) and TiO₂(r)(110) causes activation barriers associated with the first-order rate constants ($k_{\text{d},1}$) to be very similar on both surfaces, in spite of their very different acid and base strengths. As surfaces become increasingly covered with *HCOO* and the co-adsorbed protons at higher HCOOH pressures, the measured rates on TiO₂(r) become about ten-fold lower than those on TiO₂(a) (Figure 3). These rates depend not only on the first-order rate constant ($k_{\text{d},1}$) but also on the K_{HCOO^*} term in the denominator of eq 1, which reflects the formation free energy of *HCOO* and a bound proton from HCOOH(g) (ΔG_{HCOO^*}). These ΔG_{HCOO^*} values and their respective enthalpic components are much more negative on TiO₂(r) than on TiO₂(a), as evident from theory ($\Delta G_{\text{HCOO}^*} = -64$ vs -42 kJ mol⁻¹ at 533 K; $\Delta H_{\text{HCOO}^*} = -149$ vs -128 kJ mol⁻¹; Table 1) and experiments ($\Delta G_{\text{HCOO}^*} = -75 \pm 1$ vs -25 ± 2 kJ mol⁻¹ at 533 K; $\Delta H_{\text{HCOO}^*} = -149 \pm 7$ vs -109 ± 7 kJ mol⁻¹; Table 1). The greater stability of *HCOO* species on TiO₂(r) accounts for the ten-fold lower rates on TiO₂(r) than on TiO₂(a) at high *HCOO* coverages (Figure 3). The stronger binding of *HCOO* and a co-adsorbed proton on TiO₂(r) reflects its stronger Ti_{5c} acid centers that bind *HCOO* through two interactions with the O-atoms in *HCOO*; such an effect is only partially compensated by the weaker single interaction between its O_{2c} center and the proton. These results illustrate reactivity rankings among catalysts depend sensitively on what determines measured rates at the conditions chosen for such comparisons.

3.4. Kinetic Irrelevance of Defect Sites in HCOOH Dehydration Turnover Rates on TiO₂. DFT-derived energies on Ti_{5c}-O_{2c} pairs agree well with measured values, confirming the involvement of Lewis acid-base site pairs as the sole active centers and precluding detectable contributions from defect sites, such as O-vacancies, that are often implicated as the active centers for HCOOH dehydration.^{45,46} Such O-vacancies can form via O* recombination in inert environments or via H₂O evolution during H₂-treatments, as Ti⁴⁺ centers reduce to Ti³⁺, especially on TiO₂(r).^{21,47,48}

The intentional formation of O-vacancies by treatment of TiO₂(r) in H₂ (20 kPa, 823 K, 1 h) led to a slight decrease in HCOOH dehydration rates (36–32 μmol g⁻¹ s⁻¹; Figure 7a); such treatments also led to lower surface areas (from 33 to 28 m² g⁻¹) but to undetectable changes in areal rates (1.1 μmol m⁻² s⁻¹). These H₂-treatments led to the appearance of pre-edge features in UV-visible spectra (Figure 7b) from d-d transitions made possible by electrons placed into d-orbitals upon Ti⁴⁺ reduction to Ti³⁺. These pre-edge features persisted during HCOOH dehydration (1.5 kPa HCOOH; 533 K; Figure S11a; Supporting Information) without detectable effects on areal reaction rates, consistent with the kinetic

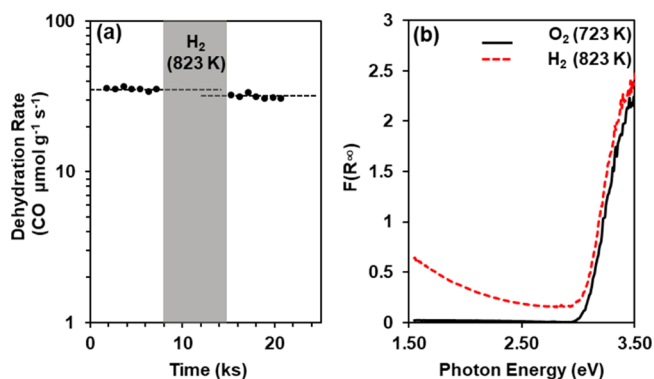


Figure 7. (a) HCOOH dehydration rates on TiO₂(r) (1.5 kPa HCOOH; 533 K) over time before and after their treatments in H₂ (20 kPa; 823 K; 1 h) and (b) UV-vis spectra of TiO₂(r) in flowing He (433 K) after their treatments in O₂ (20 kPa; 723 K; 15 h) or H₂ (20 kPa; 823 K; 1 h).

irrelevance of such defect sites; these featured disappeared upon contact with O₂ (20 kPa, 573 K; Figure S11b; Supporting Information) as Ti³⁺ centers convert to Ti⁴⁺. The absence of detectable effects of reduced centers on rates may reflect their predominant presence at subsurface layers or their irreversible titration by HCOOH-derived species during catalysis.

DFT-derived enthalpies for HCOOH dissociation at O-vacancies on TiO₂(r)(110) (−210 kJ mol⁻¹; geometries in Figure S5; Supporting Information) indicate the formation of very stable *HCOO* species that titrate O-vacancies through concerted interactions with vicinal Ti_{5c} centers. Such species decompose with large activation barriers (+187 kJ mol⁻¹; the TS structure in Figure S6; Supporting Information), consistent with the blockage of O-vacancies by *HCOO* at conditions of HCOOH dehydration catalysis.

The proposal that O-vacancies act as essential active centers for HCOOH dehydration merely reflects the observation that only such sites are able to retain bound HCOOH-derived species up to decomposition temperatures in inert environments. The presence of HCOOH(g) during steady-state catalysis allows the involvement of HCOOH* and *HCOO* that act as competent reactive intermediates at Ti_{5c}–O_{2c} pairs, but otherwise desorb before decomposition in inert environments.

3.5. Mechanistic Implications and Rate Estimates for HCOOH Formation from CO–H₂O Reactants. The mechanistic insights and rate measurements described earlier for HCOOH dehydration allow quantitative inferences about the rate of the reverse reaction through De Donder formalisms of nonequilibrium thermodynamics.^{49,50} Such CO–H₂O conversion rates to HCOOH are not accessible to direct measurements at relevant conditions because of unfavorable thermodynamics (ΔG_{533K} = +47 kJ mol⁻¹).⁵¹ The formation of HCOOH from CO–H₂O (or CO₂–H₂) reactants may provide a molecular shuttle that enables bifunctional WGS and methanol synthesis turnovers without the requirement for atomic contact among functions.

HCOOH dehydration turnovers at Ti_{5c}–O_{2c} pairs on TiO₂ surfaces are governed by only one kinetically relevant step (step 3a; Scheme 1), allowing the reverse CO–H₂O conversion rates to be rigorously expressed from the reverse sequence of elementary steps (in Scheme 1).^{24,25} These rates (per Ti_{5c}–O_{2c}; r_h) on sparsely covered surfaces are given by

$$r_h = k_h K_{H/OH} P_{H_2O(g)} P_{CO(g)} = k_{h,1} P_{H_2O(g)} P_{CO(g)} \quad (6)$$

which accurately describes the rates as long as bare Ti_{5c}–O_{2c} centers remain as the most abundant surface intermediates (derivation details in Section S5.3; Supporting Information). The CO hydration rate constant, k_{h,1}, reflects the free energy of the kinetically relevant TS (involved in step 3a; Scheme 1; G_d[‡]) referenced to CO(g) and H₂O(g) precursors (ΔG_{h,1}[‡])

$$\begin{aligned} k_{h,1} &= \frac{k_B T}{h} \exp\left(\frac{-(G_d^\ddagger - G_{CO(g)} - G_{H_2O(g)})}{RT}\right) \\ &= \frac{k_B T}{h} \exp\left(\frac{-(\Delta G_{h,1}^\ddagger)}{RT}\right) \end{aligned} \quad (7)$$

The free energy of this TS (G_d[‡]) relative to HCOOH(g) (ΔG_{d,1}[‡]) is reflected in the k_{d,1} constant for the forward HCOOH dehydration (via eq 3). Consequently, the ΔG_{h,1}[‡] values (and thus k_{h,1} constants and CO–H₂O conversion rates) can be explicitly calculated from the measured ΔG_{d,1}[‡] values (in Table 1) and thermodynamics of gas-phase molecules [HCOOH(g), CO(g), and H₂O(g)]

$$\begin{aligned} \Delta G_{h,1}^\ddagger &= G_d^\ddagger - G_{CO(g)} - G_{H_2O(g)} \\ &= \Delta G_{d,1}^\ddagger + (G_{HCOOH(g)} - G_{CO(g)} - G_{H_2O(g)}) \end{aligned} \quad (8)$$

Estimated activation free energy, enthalpy, and entropy associated with the rate constants for the reverse CO hydration routes (k_{h,1}; eq 6) are listed in Table 4 for TiO₂(a) and

Table 4. Activation Free Energies, Enthalpies and Entropies Associated with the Rate Constants for the CO Hydration Routes, k_{h,1} (=K_{H/OH}*k_h; in Eq 8) for TiO₂(a) and TiO₂(r)^a

k _{h,1} (=K _{H/OH} *k _h)	TiO ₂ (a)	TiO ₂ (r)
ΔG _{h,1} [‡] (kJ mol ⁻¹) at 533 K	+156 ± 1	+141 ± 1
ΔH _{h,1} [‡] (kJ mol ⁻¹)	−6 ± 3	−8 ± 5
ΔS _{h,1} [‡] (J K ⁻¹ mol ⁻¹)	−305 ± 6	−280 ± 9

^aThese values are estimated via eq 8. Free energies of gas-phase molecules are taken from the NIST database.⁵¹ Uncertainties reflect 95% confidential intervals for the estimation of ΔG_{d,1}[‡], ΔH_{d,1}[‡] and ΔS_{d,1}[‡] values in Table 1.

TiO₂(r) catalysts. The activation entropies for CO–H₂O conversions are very large and negative (ΔS_{h,1}[‡] = −305 ± 6 J K⁻¹ mol⁻¹ for TiO₂(a) and −280 ± 9 J K⁻¹ mol⁻¹ for TiO₂(r); Table 4), reflecting the entropic cost required to bring together two gas-phase molecules, CO(g) and H₂O(g), to form the kinetically relevant TS. The activation barriers are nearly zero and similar between TiO₂(a) and TiO₂(r) catalysts (ΔH_{d,1}[‡] = −6 ± 3 and −8 ± 5 kJ mol⁻¹, respectively; Table 4) because Ti_{5c}–O_{2c} pairs at TiO₂(a) and TiO₂(r) surfaces stabilize the TS to a similar extent. These analyses, in turn, provide predictions that the CO formation routes are much more favorable at lower temperatures; therefore, promotional effects by oxides may be maximized at lower temperatures if HCOOH molecules formed on these oxides are involved as reactive intermediates in WGS or methanol synthesis via tandem reactions.

4. CONCLUSIONS

HCOOH dehydration turnover rates were measured on TiO₂(a) (513–553 K) and TiO₂(r) (533–563 K) crystalline

powders at a range of HCOOH pressures (0.03–3 kPa); these conditions were chosen to ensure the access of $\text{Ti}_{5c}\text{-O}_{2c}$ pairs by bound reactive intermediates, the prerequisite to assess the acid–base properties of such pairs for HCOOH dehydration catalysis. Measured rates and KIEs were analyzed in terms of elementary steps for HCOOH dehydration and corresponding rate parameters, which, in turn, allowed rigorous comparisons to DFT-derived values. These results are combined to show that HCOOH dehydration elementary steps on TiO_2 surfaces involve the concurrent activation of C–O and C–H bonds in a molecularly bound HCOOH (HCOOH^*) by a $\text{Ti}_{5c}\text{-O}_{2c}$ pair at the kinetically relevant step. The TS mediating this step contains the OH group in HCOOH^* that is nearly added on the Ti_{5c} center and the H-atom in its C–H group that is nearly added on the vicinal O_{2c} center. Such concurrent involvement of acid and base centers at the kinetically relevant step and the late character of the relevant TS render dissociative H_2O adsorption energy at a $\text{Ti}_{5c}\text{-O}_{2c}$ pair as a more appropriate descriptor for dehydration reactivity than the independent strength of acid and base sites. The stronger Lewis acid strengths of Ti_{5c} centers in $\text{TiO}_2(\text{r})(110)$ are nearly completely compensated by the weaker base strengths of its O_{2c} centers, leading to similar dissociative H_2O adsorption energies at $\text{Ti}_{5c}\text{-O}_{2c}$ pairs on $\text{TiO}_2(\text{a})(101)$ and $\text{TiO}_2(\text{r})(110)$ surfaces. Such a balance causes activation barriers associated with the first-order HCOOH dehydration rate constants to be very similar on both surfaces, in spite of their very different acid and base properties.

The O–H activation in HCOOH^* forms $^*\text{HCOO}^*$ and a bound proton at a vicinal O_{2c} center, which present as the most abundant surface species on TiO_2 surfaces during HCOOH dehydration catalysis. A direct C–O and C–H activation in $^*\text{HCOO}^*$, however, requires a very large barrier, rendering such route kinetically inaccessible at relevant conditions. $^*\text{HCOO}^*$ and the co-adsorbed proton, instead, recombine to form its more weakly bound precursor, HCOOH^* , which provides a route to the CO products with much lower barriers.

The proposed HCOOH dehydration pathways on $\text{Ti}_{5c}\text{-O}_{2c}$ site pairs are in full accord with all experimental observations and theoretical calculations without invoking defects as active sites. This kinetic and thermodynamic information from HCOOH dehydration is used to derive rates, activation energy, and activation entropy of the reverse CO hydration route on $\text{Ti}_{5c}\text{-O}_{2c}$ pairs at bare TiO_2 surfaces. These results, in turn, show how Lewis acid–base pairs of moderate strengths provide high HCOOH dehydration reactivity (and by reversibility inferences also high rates for $\text{CO-H}_2\text{O}$ reactions) through the balance between the acid and base centers.

■ ASSOCIATED CONTENT

Supporting Information

The Supporting Information is available free of charge at <https://pubs.acs.org/doi/10.1021/acs.jpcc.0c05721>.

Assessment of internal mass transfer limitation within TiO_2 particles; first-order fittings of TPSR; effects of CO and H_2O pressures on dehydration turnover rates; DFT-derived geometries for intermediates and TS involved in direct $^*\text{HCOO}^*$ decomposition route; derivation of rate equations; kinetic parameter optimizations; parity plots and Arrhenius plots for the rate parameters; and in situ UV–vis spectra of H_2 -treated $\text{TiO}_2(\text{r})$ samples during HCOOH and O_2 reactions (PDF)

■ AUTHOR INFORMATION

Corresponding Author

Enrique Iglesia – Department of Chemical and Biological Engineering, University of California, Berkeley, Berkeley, California 94720, United States; orcid.org/0000-0003-4109-1001; Email: iglesia@berkeley.edu

Authors

Stephanie Kwon – Department of Chemical and Biological Engineering, University of California, Berkeley, Berkeley, California 94720, United States; Department of Chemical and Biological Engineering, Colorado School of Mines, Golden, Colorado 80401, United States

Ting Chun Lin – Department of Chemical and Biological Engineering, University of California, Berkeley, Berkeley, California 94720, United States; Department of Chemical Engineering and Materials Science, University of Minnesota–Twin Cities, Minneapolis, Minnesota 55455, United States

Complete contact information is available at:

<https://pubs.acs.org/doi/10.1021/acs.jpcc.0c05721>

Notes

The authors declare no competing financial interest.

■ ACKNOWLEDGMENTS

The authors thank Sancialita Sathiyamoorthy at UC Berkeley for her help in measuring UV–vis spectra. We also thank Haefa Mansour, Ava Hejazi, and Dr. De-La-Torre at UC Berkeley for their careful proofreading of the manuscript. This work has been supported by the U.S. Department of Energy (DOE), Office of Science, Office of Basic Energy Sciences (contract no. DE-AC05-76RL0-1830). This research was achieved using computational resources at the National Energy Research Scientific Computing Center (NERSC), a U.S. Department of Energy, Office of Science, User Facility operated under contract no. DE-AC02-05CH1123.

■ REFERENCES

- (1) Qiao, J.; Liu, Y.; Hong, F.; Zhang, J. A Review of Catalysts for the Electroreduction of Carbon Dioxide to Produce Low-Carbon Fuels. *Chem. Soc. Rev.* **2014**, *43*, 631.
- (2) Ueno, A.; Onishi, T.; Tamaru, K. Dynamic Technique to Elucidate the Reaction Intermediate in Surface Catalysis. Water-Gas Shift Reaction. *Faraday Soc. Trans.* **1970**, *66*, 756–763.
- (3) Robbins, J. L.; Iglesia, E.; Kelkar, C. P.; DeRites, B. Methanol Synthesis over Cu/SiO₂ Catalysts. *Catal. Lett.* **1991**, *10*, 1–10.
- (4) Yang, Y.; Mei, D.; Peden, C. H. F.; Campbell, C. T.; Mims, C. A. Surface-Bound Intermediates in Low-Temperature Methanol Synthesis on Copper: Participants and Spectators. *ACS Catal.* **2015**, *5*, 7328–7337.
- (5) Iglesia, E.; Michel, B. Unimolecular and Bimolecular Formic Acid Decomposition on Copper. *J. Phys. Chem.* **1986**, *20*, 5272–5274.
- (6) Iglesia, E.; Boudart, M. Decomposition of Formic-Acid on Copper, Nickel, and Copper Nickel-Alloys .1. Preparation and Characterization of Catalysts. *J. Catal.* **1983**, *81*, 204–213.
- (7) Ojeda, M.; Iglesia, E. Formic Acid Dehydrogenation on Au-Based Catalysts at Near-Ambient Temperatures. *Angew. Chem.* **2009**, *121*, 4894–4897.
- (8) Scaranto, J.; Mavrikakis, M. Density Functional Theory Studies of HCOOH Decomposition on Pd(111). *Surf. Sci.* **2016**, *650*, 111–120.
- (9) Scaranto, J.; Mavrikakis, M. HCOOH Decomposition on Pt(111): A DFT Study. *Surf. Sci.* **2016**, *648*, 201–211.

- (10) Noto, Y.; Fukuda, K.; Onishi, T.; Tamaru, K. Mechanism of Formic Acid Decomposition over Dehydrogenation Catalysts. *Faraday Soc. Trans.* **1967**, *63*, 3081–3087.
- (11) Fukuda, K.; Noto, Y.; Onishi, T.; Tamaru, K. Mechanism of Dehydration Decomposition of Formic Acid over Alumina and Silica. Adsorption Measurements during the Catalytic Reaction. *Trans. Faraday Soc.* **1967**, *63*, 3072.
- (12) Henderson, M. A. Complexity in the Decomposition of Formic Acid on the TiO₂ (110) Surface. *J. Phys. Chem. B* **1997**, *101*, 221–229.
- (13) Kwon, S.; Lin, T. C.; Iglesia, E. Elementary Steps and Site Requirements in Formic Acid Dehydration Reactions on Anatase and Rutile TiO₂ Surfaces. *J. Catal.* **2020**, *383*, 60–76.
- (14) Mars, P.; Scholten, J. J. F.; Zwietering, P. The Catalytic Decomposition of Formic Acid. *Adv. Catal.* **1963**, *14*, 35–113.
- (15) Senanayake, S. D.; Mullins, D. R. Redox Pathways for HCOOH Decomposition over CeO₂ Surfaces. *J. Phys. Chem. C* **2008**, *112*, 9744–9752.
- (16) Munuera, G. Study of the Mechanisms of Formic Acid Dehydration on TiO₂. *J. Catal.* **1970**, *18*, 19–29.
- (17) Shekhar, M.; Wang, J.; Lee, W.-S.; Williams, W. D.; Kim, S. M.; Stach, E. A.; Miller, J. T.; Delgass, W. N.; Ribeiro, F. H. Size and Support Effects for the Water-Gas Shift Catalysis over Gold Nanoparticles Supported on Model Al₂O₃ and TiO₂. *J. Am. Chem. Soc.* **2012**, *134*, 4700–4708.
- (18) Panagiotopoulou, P.; Kondarides, D. I. Effect of the Nature of the Support on the Catalytic Performance of Noble Metal Catalysts for the Water-Gas Shift Reaction. *Catal. Today* **2006**, *112*, 49–52.
- (19) Huff, C. A.; Sanford, M. S. Cascade Catalysis for the Homogeneous Hydrogenation of CO₂ to Methanol. *J. Am. Chem. Soc.* **2011**, *133*, 18122–18125.
- (20) Chen, Y.; Choi, S.; Thompson, L. T. Low-Temperature CO₂ Hydrogenation to Liquid Products via a Heterogeneous Cascade Catalytic System. *ACS Catal.* **2015**, *5*, 1717–1725.
- (21) Diebold, U. The Surface Science of Titanium Dioxide. *Surf. Sci. Rep.* **2003**, *48*, 53–229.
- (22) Lazzeri, M.; Vittadini, A.; Selloni, A. Structure and Energetics of Stoichiometric TiO₂ Anatase Surfaces. *Phys. Rev. B: Condens. Matter Mater. Phys.* **2001**, *63*, 155409.
- (23) Wang, S.; Iglesia, E. Experimental and Theoretical Assessment of the Mechanism and Site Requirements for Ketonization of Carboxylic Acids on Oxides. *J. Catal.* **2017**, *345*, 183–206.
- (24) Gounder, R.; Iglesia, E. Catalytic Hydrogenation of Alkenes on Acidic Zeolites: Mechanistic Connections to Monomolecular Alkane Dehydrogenation Reactions. *J. Catal.* **2011**, *277*, 36–45.
- (25) Gounder, R.; Iglesia, E. Catalytic Alkylation Routes via Carbonium-Ion-Like Transition States on Acidic Zeolites. *ChemCatChem* **2011**, *3*, 1134–1138.
- (26) Brunauer, S.; Emmett, P. H.; Teller, E. Adsorption of Gases in Multimolecular Layers. *J. Am. Chem. Soc.* **1938**, *60*, 309–319.
- (27) Stull, D. R. Vapor Pressure of Pure Substances. Organic and Inorganic Compounds. *Ind. Eng. Chem.* **1947**, *39*, 517–540.
- (28) Bridgeman, O. C.; Aldrich, E. W. Vapor Pressure Tables for Water. *J. Heat Transfer* **1964**, *86*, 279.
- (29) Mirabella, F. M. *Modern Techniques in Applied Molecular Spectroscopy*; John Wiley & Sons, Inc., 1998.
- (30) Perdew, J. P.; Burke, K.; Ernzerhof, M. Generalized Gradient Approximation Made Simple. *Phys. Rev. Lett.* **1996**, *77*, 3865–3868.
- (31) Kresse, G.; Hafner, J. Ab Initio Molecular-Dynamics Simulation of the Liquid-Metal–Amorphous-Semiconductor Transition in Germanium. *Phys. Rev. B: Condens. Matter Mater. Phys.* **1994**, *49*, 14251–14269.
- (32) Kresse, G.; Furthmüller, J. Efficient Iterative Schemes for Ab Initio Total-Energy Calculations Using a Plane-Wave Basis Set. *Phys. Rev. B: Condens. Matter Mater. Phys.* **1996**, *54*, 11169–11186.
- (33) Kresse, G.; Furthmüller, J. Efficiency of Ab-Initio Total Energy Calculations for Metals and Semiconductors Using a Plane-Wave Basis Set. *Comput. Mater. Sci.* **1996**, *6*, 15–50.
- (34) Blöchl, P. E. Projector Augmented-Wave Method. *Phys. Rev. B: Condens. Matter Mater. Phys.* **1994**, *50*, 17953–17979.
- (35) Grimme, S. Semiempirical GGA-Type Density Functional Constructed with a Long-Range Dispersion Correction. *J. Comput. Chem.* **2006**, *27*, 1787–1799.
- (36) Mills, G.; Jónsson, H.; Schenter, G. K. Reversible Work Transition State Theory: Application to Dissociative Adsorption of Hydrogen. *Surf. Sci.* **1995**, *324*, 305–337.
- (37) Henkelman, G.; Jónsson, H. A Dimer Method for Finding Saddle Points on High Dimensional Potential Surfaces Using Only First Derivatives. *J. Chem. Phys.* **1999**, *111*, 7010–7022.
- (38) Donald, A. McQuarrie. *Statistical Mechanics*; University Science Books: Sausalito, CA, 2000.
- (39) Campbell, C. T.; Sellers, J. R. V. Enthalpies and Entropies of Adsorption on Well-De Fined Oxide Surfaces: Experimental Measurements. *Chem. Rev.* **2013**, *113*, 4106–4135.
- (40) Miller, K. L.; Lee, C. W.; Falconer, J. L.; Medlin, J. W. Effect of Water on Formic Acid Photocatalytic Decomposition on TiO₂ and Pt/TiO₂. *J. Catal.* **2010**, *275*, 294–299.
- (41) Vittadini, A.; Selloni, A.; Rotzinger, F. P.; Grätzel, M. Formic Acid Adsorption on Dry and Hydrated TiO₂ Anatase (101) Surfaces by DFT Calculations. *J. Phys. Chem. B* **2000**, *104*, 1300–1306.
- (42) Miller, K. L.; Falconer, J. L.; Medlin, J. W. Effect of Water on the Adsorbed Structure of Formic Acid on TiO₂ Anatase (101). *J. Catal.* **2011**, *278*, 321–328.
- (43) Tabacchi, G.; Fabbiani, M.; Mino, L.; Martra, G.; Fois, E. The Case of Formic Acid on Anatase TiO₂(101): Where Is the Acid Proton? *Angew. Chem. Int. Ed.* **2019**, *58*, 12431–12434.
- (44) Janik, M. J.; Macht, J.; Iglesia, E.; Neurock, M. Correlating Acid Properties and Catalytic Function: A First-Principles Analysis of Alcohol Dehydration Pathways on Polyoxometalates. *J. Phys. Chem. C* **2009**, *113*, 1872–1885.
- (45) Morikawa, Y.; Takahashi, I.; Aizawa, M.; Namai, Y.; Sasaki, T.; Iwasawa, Y. First-Principles Theoretical Study and Scanning Tunneling Microscopic Observation of Dehydration Process of Formic Acid on a TiO₂(110) Surface. *J. Phys. Chem. B* **2004**, *108*, 14446–14451.
- (46) Aizawa, M.; Morikawa, Y.; Namai, Y.; Morikawa, H.; Iwasawa, Y. Oxygen Vacancy Promoting Catalytic Dehydration of Formic Acid on TiO₂ (110) by in Situ Scanning Tunneling Microscopic Observation. *J. Phys. Chem. B* **2005**, *109*, 18831–18838.
- (47) Cheng, H.; Selloni, A. Energetics and Diffusion of Intrinsic Surface and Subsurface Defects on Anatase TiO₂(101). *J. Chem. Phys.* **2009**, *131*, 054703.
- (48) Cheng, H.; Selloni, A. Surface and Subsurface Oxygen Vacancies in Anatase TiO₂ and Differences with Rutile. *Phys. Rev. B* **2009**, *79*, 092101.
- (49) De Donder, T.; Van Rysselberghe, P. Thermodynamic Theory of Affinity. *A Book of Principles*; Stanford University, Stanford University Press: California, 1937.
- (50) Boudart, M. Some Applications of the Generalized De Donder Equation to Industrial Reactions. *Ind. Eng. Chem. Fundam.* **1986**, *25*, 70–75.
- (51) *The NIST Standard Reference Database.*